

Diese Arbeit wurde vorgelegt am
Lehr- und Forschungsgebiet Theorie der hybriden Systeme

**Unsicherheits-Quantifizierung und Multikriterielle
Optimierung von Windparks**
**Uncertainty Quantification and Multi-Objective
Optimization of Wind Farms**

Bachelorarbeit
Informatik

März 2019

Vorgelegt von Presented by	Julian Düstersiek Weberstr. 5 52064 Aachen Matrikelnummer: 345316 julian.duestersiek@rwth-aachen.de
Erstprüfer First examiner	Prof. Dr. rer. nat. Erika Ábrahám Lehr- und Forschungsgebiet: Theorie der hybriden Systeme RWTH Aachen University
Zweitprüfer Second examiner	Prof. Dr. rer. nat. Thomas Noll Software Modeling and Verification Group RWTH Aachen University
Externer Betreuer External supervisor	Dr. rer. nat. Pascal Richter Steinbuch Centre for Computing Karlsruhe Institute of Technology

Eigenständigkeitserklärung

Hiermit versichere ich, dass ich diese Bachelorarbeit selbständig verfasst und keine anderen als die angegebenen Quellen und Hilfsmittel benutzt habe. Die Stellen meiner Arbeit, die dem Wortlaut oder dem Sinn nach anderen Werken entnommen sind, habe ich in jedem Fall unter Angabe der Quelle als Entlehnung kenntlich gemacht. Dasselbe gilt sinngemäß für Tabellen und Abbildungen. Diese Arbeit hat in dieser oder einer ähnlichen Form noch nicht im Rahmen einer anderen Prüfung vorgelegen.

Aachen, im März 2019

Julian Düstersiek

Contents

List of Figures	V
List of Tables	VI
1 Introduction	1
2 Related Works	2
2.1 Simulation of Wake Effect	2
2.2 Optimization of Wind Farm Layouts	2
3 Model	3
3.1 Wind Model	3
3.1.1 Weibull Distribution	3
3.2 Wake Model	4
3.3 Power Generation Model	8
3.4 Gross Annual Energy Production	8
3.5 Time-dependent Annual Energy Production	10
3.6 Cost Model	10
3.6.1 Net Annual Energy Production	11
3.6.2 Levelized Cost of Electricity	11
3.6.3 Net Present Value	12
3.6.4 Internal Rate of Return	12
3.7 Tariff Consideration	13
4 AEP of Raw Data	15
4.0.1 Nearest Neighbour Interpolation	17
4.0.2 Bilinear Interpolation	17
4.1 Results	19
5 Wind Farm Modelling with Uncertainties	22
5.1 Uncertain parameters	22
5.2 Stochastic Model	22
5.2.1 Uncertain Wind Model	23
5.2.2 Uncertain Wake Model	23
5.2.3 Uncertain Power Generation	24
5.2.4 Uncertain Gross Annual Energy Production	24
5.2.5 Uncertain Net Annual Energy Production	25
5.2.6 Uncertain Levelized Cost of electricity	25
5.2.7 Uncertain Net Present Value	25
5.2.8 Uncertain Internal Rate of Return	25
6 Multilevel-Monte Carlo Methods	26
6.1 Monte Carlo	26

6.2	Quasi-Monte Carlo	28
6.3	Multilevel-Monte Carlo	29
6.4	Quasi-Multilevel-Monte Carlo	31
7	Multi-Objective Optimization	32
7.1	Objective Functions	32
7.1.1	Annual Energy Production Efficiency	33
7.1.2	UQ Variance	33
7.1.3	LCOE with Cabling	34
7.1.4	Noise Model	37
7.2	Pareto Frontier	39
7.2.1	Local Search	40
7.3	Results	41
7.4	Performance on Real World Wind Farms	45
7.4.1	Horns Rev 1	46
7.4.2	Sandbank	47
7.4.3	DanTysk	48
8	Conclusion and Future Works	50
	References	51

List of Figures

1	General overview of the simulation model.	3
2	Wind direction probabilities of FINO3 wind measurement data.	4
3	Approximated wind speed distribution as Weibull distribution.	5
4	Construction and measurements of a wind turbine.	6
5	Visualization of the wake effect.	7
6	Partial wake effect on turbines.	8
7	Thrust coefficient and power production of a turbine.	9
8	Time-dependent wind direction probabilities.	11
9	Optimized turbine layouts with different tariff settings.	14
10	Weibull approximation and original FINO3 measurement comparison. . .	15
11	Heat map of simulated AEP output.	16
12	Amount visualization of FINO3 data pairs with different discretizations.	16
13	Nearest Neighbour combination of simulated power and wind data pair occurrences.	18
14	Interpolated combination of simulated power and wind data pair occurrences.	18
15	Investigation of the wind speed resolution with a constant number of wind directions.	20
16	Evaluation of wind direction resolution with a constant wind speed interval.	20
17	Fitted Weibull distribution with maximum likelihood estimation. . . .	23
18	Perturbed C_t and power curve of a turbine.	24
19	Example of random number generator compared to the Sobel generator.	27
20	Convergence study of the Multi-level Monte Carlo method.	29
21	Convergence study of the QMLMC method with different epsilon values.	30
22	Investigation of variance using different turbine layouts.	34
23	Overview of the different cable distributor stations on- and off-shore. .	35
24	Example of the effect of cable optimization on a real world offshore wind farm.	36
25	Effects of distance on noise level observed over a whole year.	38
26	Simulated turbine positions of the local search for one iteration step. .	41
27	Evaluation of Pareto optima with AEP value and noise effect for different numbers of turbines.	43
28	Evaluation of Pareto optima with AEP value and LCOE for different numbers of turbines.	43
29	Examination of the Pareto optimum with three objective functions plotted in a 2D graph.	45
30	Multi-objective optimization for Horns Rev 1	47
31	Multi-objective optimization for Sandbank	48
32	Multi-objective optimization for DanTysk	49

List of Tables

1	Settings for time-dependent Tariff.	13
2	Uncertain input parameters and their influencing factors.	22
3	AEP and variance results evaluation at different turbine layouts.	34
4	Breakdown of the various costs of installing cables in an offshore wind farm.	37
5	Information for the different test cases to evaluate the multi-objective optimizer.	42
6	Settings for the investigation of the multi-objective optimizer with three target functions.	44
7	Simulation results of different cost models with original turbine layouts for the three real-world wind farms.	46

1 Introduction

The climate change is one of the biggest environmental struggles in this century. The industrial revolution has left its traces, and now it is important to counteract the climatic problems with renewable energies. Big steps have already been taken to reduce CO₂ emissions, but there is still a long way to go before the whole world has switched to renewable, so-called green energy.

Solar and wind energy are the leading forms of renewable energy production. Wind is one of the universal forms, as it is always present compared to solar energy, which can only be used efficiently in certain parts of the world and not at night.

Therefore wind farms have the potential to become the worlds leading energy source. To reduce costs, the wind turbines are clustered into wind farms and are subdivided in onshore and offshore wind farms. The difference is that onshore wind farms are built on land, while offshore wind farms are built on underwater areas near the coast.

Onshore wind farms are characterised by lower investment and maintenance costs and easier access to the generated energy, but environmental conditions reduce the turbine efficiency. In addition, the noise factor of turbines is the focus of public discussions. Offshore wind farms, on the other hand, have higher investment and maintenance costs because they are built in the hard-to-reach sea. The energy produced is also more distant from the region in which it is needed. But in the longer term, the offshore version has some advantages. On the sea, a much stronger wind dominates in comparison to the wind on land, which increases the total power. There are also no hurdles through mountains, hills, etc. that disturb the wind, which in turn leads to higher energy production. There is also more space available on the sea so that bigger wind farms can be build.

The topics of this thesis can be categorized into three parts. The first part deals with the model aspects, i.e. the simulation, and the calculation of the most important attribute of a wind farm, the energy produced over a whole year.

In the second part different methods for the investigation of uncertainties are introduced. It has to be considered which uncertainties in the construction of a wind farm can lead to a misinterpretation of the whole project. The main focus is on a stable estimated result for the energy production with uncertainties.

The last part deals with the optimization of turbine layouts. However, the aim is not only to achieve the best energy production with a single-objective optimizer, instead a multi-objective optimizer is introduced which can handle several optimization goals. The purpose is not one specific optimal result, but a set of optima from which to choose according to need.

2 Related Works

In this section some known approaches and recent work in the field of the *wind farm layout optimization problem* (*WFLOP*) are mentioned. Here we focus on wake models and optimization algorithms as the main components of this thesis.

2.1 Simulation of Wake Effect

In order to carry out an optimization, a suitable simulation must first be created, and the choice of a suitable wake model is decisive. For this modelling of the wake effect there were already many approaches in the last years. One of the first and most significant publications was the *Jensen model* [22, 23], also known as the *PARK* model, with its variant known as *Modified PARK*.

This model has gained in popularity and importance because it has a simple basic principle and is available in different versions. The wake model is popular as an engineering wind turbine wake model for simulating the reduction of the wind speed downstream. It is also the base of the *PARK* model, which was developed for the calculations of the Wind Atlas Analysis and Application Program (WAsP). WAsP is widely used for the estimation of wind resources. However, many of today's approaches are based on the models of Jensen.

2.2 Optimization of Wind Farm Layouts

Already in the late eighties it was recognized that the efficiency and thus also the profit of a wind farm can be improved by optimizing the wind turbine positions. One of the decisive factors for this was the work of Mosetti et al. in 1994 [30]. By use of a so-called *genetic algorithm* Mosetti et al. created a solid first approach to solve the WFLOP. This method is inspired by nature and is a population-based metaheuristic that mimics the phenomena of natural selection to produce better results over a number of iterations.

Building on this idea, is also one of the latest approaches published by Roscher et al. in 2018 [37]. The authors use the *linear Jensen model* to simulate the wake effect and an adapted financial model to be able to minimize costs by optimization. The genetic algorithm used works with the influence of a random variable to find the approximated global optimum instead of the local optimum. Furthermore, the authors perform a multi-objective optimization, i.e. an optimization with several functions. A weighted approach is used which combines the various functions into one. The aim is to achieve one optimum value target with specific allocation of weighting parameters. The objective functions used are the power value of the wind farm and a reduction of costs by choosing the optimal lift height and rotor diameter.

3 Model

In this section the different parts of an wind farm model will be described which is largely bases on the work of Heiming [20]. At first, the wind model with related data and the resulting wake model will be explained. Then, the power generation model will be presented to calculate the gross annual energy production (AEP). Finally, the cost model by Cakar [8] will be introduced to compare it with the cost model of Roscher [37]. The cost model consists of the net annual energy production, the levelized cost of electricity (LCOE), the net present value (NPV) and the internal rate of return (IRR). The overall model structure is shown in Figure 1.

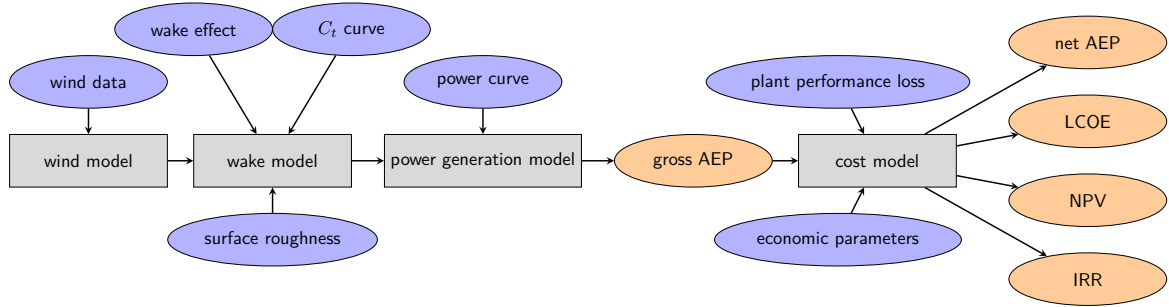


Figure 1: General overview of the simulation model presented in this thesis introduced by Richter [34]. Contains the input parameters (purple), the general models used (grey) and the output functions (orange).

3.1 Wind Model

A sufficient wind model requires large amounts of measurement data. This data reproduces the real world climate conditions for a specific area and time period. Our wind model bases on the wind data of the FINO3 research platform¹ and consists out of thousands of measurements over seven years. FINO3 is located 80 kilometres west of Sylt in the North Sea. Figure 2 shows the processed wind data divided into 12, 32 and 360 sectors which represent the probability that a wind direction from that sector occurs.

3.1.1 Weibull Distribution

To approximate the wind speed a Weibull distribution of the raw wind data is used and calculated with the maximum likelihood estimation as described by Heiming [20]. The Weibull distribution is a continuous probability distribution and has the advantage that different wind speed levels of measured wind data can be approximated very well by only two parameters. Heiming [20] noted higher speeds are less likely and the

¹<http://www.fino3.de/>

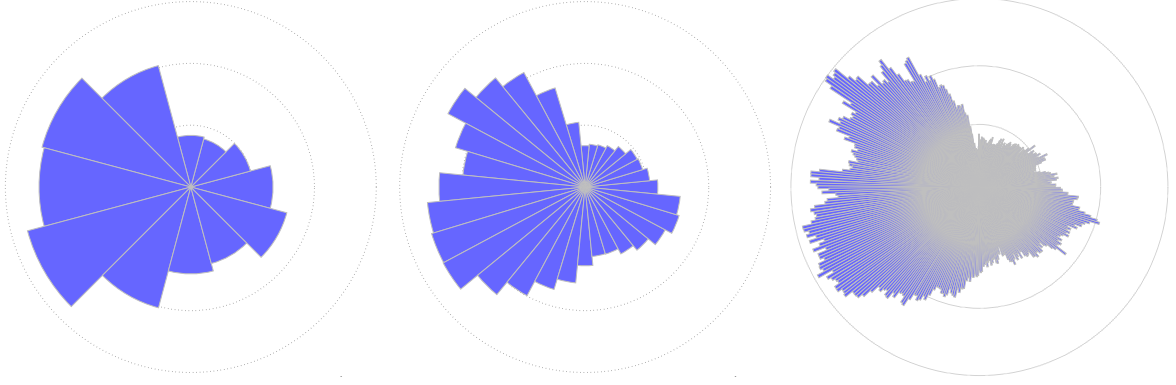


Figure 2: Combined wind direction distribution at the FINO3 research platform over the years of July 2010 to July 2018 at a measured height of 100 meter. Clustered probabilities into 12, 32 and 360 direction sectors.

probability of negative wind speeds is equal to zero.

The estimated maximum likelihood estimation is defined as

$$f_{\alpha_i}(u) = \left(\frac{k}{\lambda}\right) \cdot \left(\frac{u}{\lambda}\right)^{k-1} \cdot \exp\left(-(u \cdot \lambda)^k\right) \quad (1)$$

where the parameters $\lambda > 0$ and $k > 0$ are the scale- and shape parameter, so that the probability $f_{\alpha_i}(u)$ for every wind speed u can be calculated. The parameters λ and k are related for each wind direction as representation. So each wind direction has its own probability and its own wind speed distribution. Figure 3 shows the wind speed distribution for the sector $\alpha_i \in [225^\circ, 255^\circ)$ of FINO3.

3.2 Wake Model

An important factor at modeling a wind farm is the wake effect. Every wind turbine has to relate the wake of neighbouring turbines while calculating their power output. The effect occurs when wind passes a turbine and gets in a strong tumble. As a consequence the wind speed behind the turbine is reduced. For this purpose the wake model is needed.

First the wind turbine has to be defined as shown in Figure 4. D represents the rotor diameter and z the hub height of a turbine. In our model there is always used a horizontal-axis wind turbine, this is the most common type.

Here we focus on a simple model based on the PARK model which is originally created by Jensen [22] and Katic et al. [23] in 1986 to approximate the wake effect. This model is well suited to wind farm simulations because of its simplicity and accuracy which was examined by Barthelmie et al. [5]. Our model approximates wind speed reduction behind a turbine on one fixed height as function of the distance x and does not compute a flow field for the exact wind velocity distribution as shown in Figure 5. The wake model is designed for long distances inside the wind farm and requires a

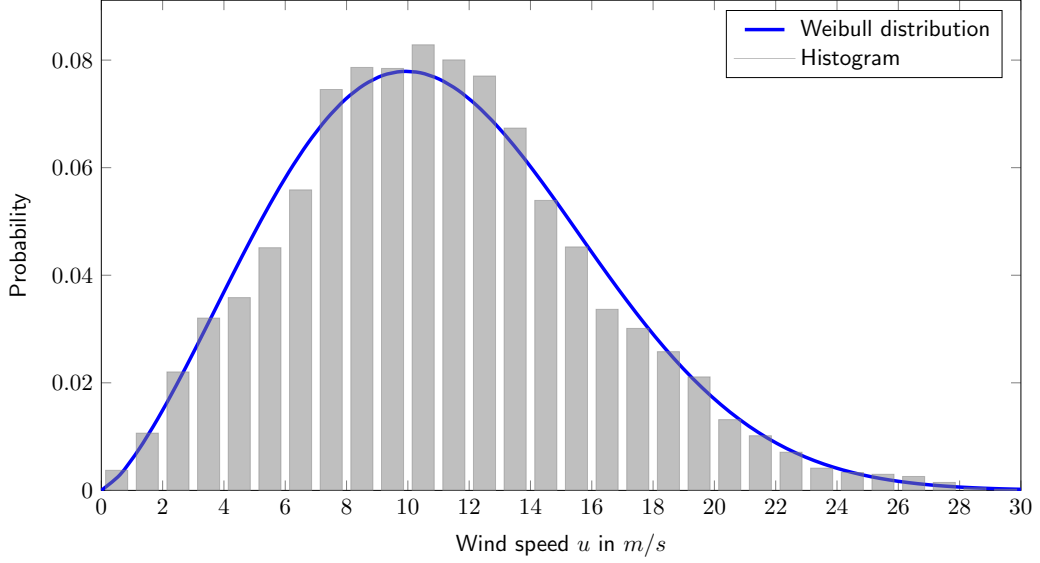


Figure 3: Approximated wind speed distribution of Richter [34] as Weibull distribution using the maximum likelihood estimation. The measured data is from the FINO3 research platform over the years of July 2010 to July 2017 for the wind direction sector $\alpha_i \in [225^\circ, 255^\circ)$. The measured wind speed distribution is illustrated as wind bins in the form of a histogram.

distance of at least three rotor diameters or more to be valid. The wake grows with a factor k defined by Samorani et al. [38] as

$$k = \frac{0.5}{\ln \frac{z}{z_0}}, \quad (2)$$

where z is again the hub height and z_0 is called surface roughness. So, the wake diameter $D_w = D_w(x)$ grows linearly by $2k$ as shown in Figure 5. The surface roughness is a variable to describe the condition of the site ground as the waves of the sea in our offshore wind farm. It can be calculated via a formula as presented in [27] depending on the sea state. However, the surface roughness $z_0 = 0.0002$ m can also be assumed as constant value which is typically for offshore sites [29].

For the derivation of velocity deficit Heiming [20] assumes conservation of momentum inside the wake and start with a balance of momentum

$$\sum \text{mass} \cdot \text{velocity} = \sum \text{density} \cdot \text{area} \cdot \text{velocity} = 0. \quad (3)$$

By assuming incompressibility of the fluid it follows

$$-\rho\pi \left(\frac{D}{2}\right)^2 u_r - \rho\pi \left(\left(\frac{D_w}{2}\right)^2 - \left(\frac{D}{2}\right)^2\right) u_0 + \rho\pi \left(\frac{D_w}{2}\right)^2 u_w = 0, \quad (4)$$

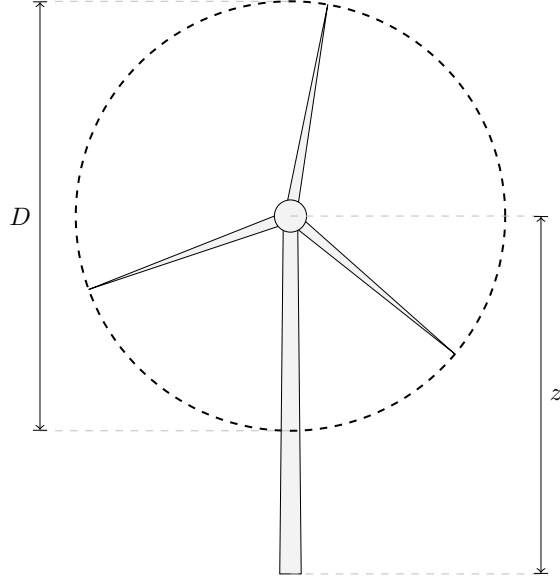


Figure 4: Construction of a horizontal-axis wind turbine and their measurements. D represents the rotor diameter and z is standing for the hub height of the mast. Source: Heiming [20]

where ρ is the air pressure, u_r is the wind speed directly behind the rotor of the turbine and u_w is the wind speed further away from the turbine inside the wake as shown in Figure 5. This can be simplified to

$$D^2 u_r + (D_w^2 - D^2) u_0 = D_w^2 u_w. \quad (5)$$

Directly behind the turbine $\delta u_r = 1 - \frac{u_r}{u_0}$ the initial velocity deficit is placed in and solved for $\frac{u_w}{u_0}$, yields

$$\frac{u_w}{u_0} = 1 - \delta u_r \left(\frac{D}{D + 2kx} \right)^2. \quad (6)$$

The initial velocity deficit δu_r will be replaced with the relative loss at the turbine

$$a(u_0) = 1 - \sqrt{1 - C_t(u_0)}, \quad (7)$$

where C_t is the thrust coefficient of the turbine. $a(u_0)$ provides us the final equation for the velocity deficit at any point inside the wake of a turbine with initial velocity u_0 .

$$\delta u(x) = 1 - \frac{u_w(x)}{u_0} = \frac{1 - \sqrt{1 - C_t(u_0)}}{\left(1 + \frac{2kx}{D}\right)^2}. \quad (8)$$

The above derivation for wind speed reduction is only applicable for the wake of a turbine in the free stream. Now we evaluate the more likely case where turbines are behind each other in wind direction. Considering two interacting turbines i and j to generalize equation (8). The first turbine i that is in front with regard to the

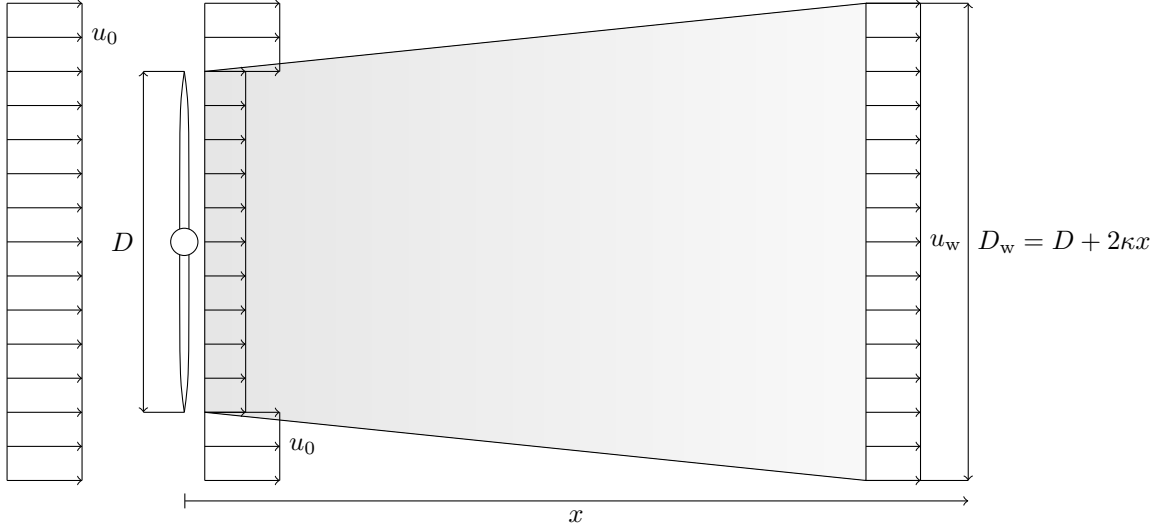


Figure 5: Visualization of the wake effect as described above. The unperturbed free stream u_0 hits the turbine and its blades, generates the wake and the resulting reduced wind speed u_w . The wake grows linear with the factor 2κ . D represents the rotor diameter of the turbine, D_w is the width of the generated wake and x stands for the distance from the turbine. Source: Heiming [20]

wind direction and the turbine j behind the first one which is affected by the wake. Otherwise j is only partly affected by the wake of i so a shadowing factor $\beta_k \in [0, 1]$ as described by Choi and Shan [9] needs to be implemented which is defined as

$$\beta_k = \frac{A_{\text{Intersection}}}{A_{\text{Turbine}}}, \quad (9)$$

where $A_{\text{Intersection}}$ is the circular part of the wake that intersects the area A_{Turbine} of turbine j which is shown in Figure 6. Equation (8) for velocity deficit has updated to

$$1 - \frac{u_w}{u_{\text{inc},i}} = \frac{\beta_k \left(1 - \sqrt{1 - C_t(u_{\text{inc},i})}\right)}{\left(1 + \frac{2\kappa x}{D}\right)^2}, \quad (10)$$

where $u_{\text{inc},i}$ is called the incident wind speed of turbine i . Till now the equation depends on incident velocity $u_{\text{inc},i}$ at turbine i . Now it needs to be transformed to make it dependent on free stream velocity u_0

$$\delta u_{ij} = 1 - \frac{u_{w,i}}{u_0} = 1 - \frac{u_{\text{inc},j}}{u_0} = \frac{u_0}{u_{\text{inc},i}} \left(\frac{\beta_k \left(1 - \sqrt{1 - C_t(u_{\text{inc},i})}\right)}{\left(1 + \frac{2\kappa x}{D}\right)^2} \right). \quad (11)$$

For the case of two interacting wakes affect one turbine j the velocity deficits are added as follows

$$\begin{aligned} \delta u_j^2 &= \delta u_{1,j}^2 + \delta u_{2,j}^2 \\ \Leftrightarrow \left(1 - \frac{u_{\text{inc},j}}{u_0}\right)^2 &= \left(1 - \frac{u_{w,1}}{u_0}\right)^2 + \left(1 - \frac{u_{w,2}}{u_0}\right)^2, \end{aligned} \quad (12)$$

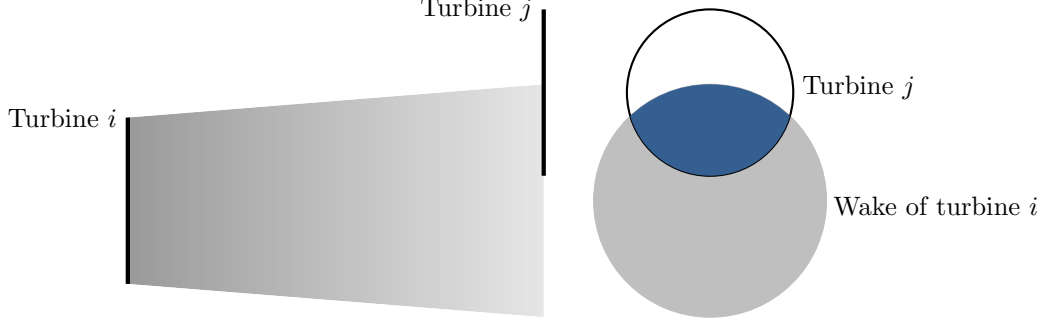


Figure 6: Visualization of the partial wake intersection according to the PARK model. The wake from turbine i crosses a section of turbine j . Source: Heiming [20]

where $u_{w,1}$ and $u_{w,2}$ are the velocities inside the two wake instances. Extended to an arbitrary number of interacting wakes δu_j can be defined as

$$\delta u_j = \sqrt{\sum_{i=1}^N \delta u_{ij}^2}, \quad (13)$$

where N is the number of interacting wakes and for each ij and δu_{ij} defines the velocity deficit caused by the wake of turbine i which affects turbine j .

3.3 Power Generation Model

In this section we consider the electrical properties of a turbine. A general wind turbine is a device that converts the kinetic energy of the wind into electrical energy. When the hub of a turbine is directed against the wind stream, the rotor blades start to rotate and the electrical generator of the turbine produces power. This power output can be represented as power curve $P(u)$. The performance descriptors depend on the wind speed. There are different types of wind turbines. As mentioned in Section 3.2 we use the most common type horizontal-axis wind turbine with three large rotor blades as shown in Figure 4. A turbine is characterized by a few more attributes. Important for our model we define for each turbine a cut-in speed u_{cutin} and a cut-out speed u_{cutout} as constraints. u_{cutin} defines the minimum wind speed that is necessary for a turbine to accomplish and produce consistent power. Contrary u_{cutout} defines the maximum wind speed a turbine can handle and work properly without getting damaged. A typically cut-in speed is about 3 to 4 m/s and the cut-out speed about 25 m/s. These are shown in Figure 7 with regard to power production and thrust coefficient. These curves depend on the air density. In this work we use a constant air density value of 1.225 kg/m^3 which corresponds to a temperature of 15°C at sea level.

3.4 Gross Annual Energy Production

In this section the calculation of the gross annual energy production $\text{AEP}_{\text{gross}}$ will be presented. The mathematical model of the AEP was introduced by Heiming [20]. For

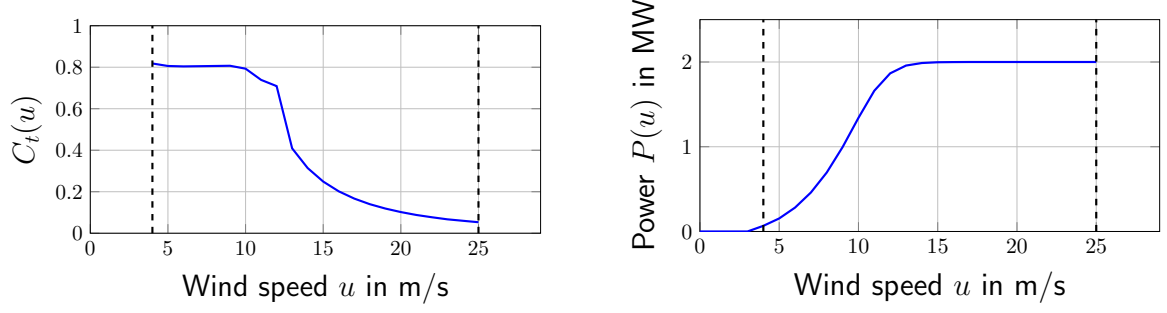


Figure 7: Thrust coefficient C_t and power production of a turbine with cut-in speed of 4 m/s and cut-out speed of 25 m/s (dashed vertical lines). Source: Cakar [8]

the calculation we define as first the expected power value P for all directions by

$$\begin{aligned}
 P &:= \int_0^{2\pi} P_\alpha d\alpha \\
 &\approx \sum_{i=1}^{N_{\text{directions}}} w_{\alpha_i} \cdot P_{\alpha_i}
 \end{aligned} \tag{14}$$

where $N_{\text{directions}}$ describing the number of wind directions and w_{α_i} standing for the weight of direction α_i . P_{α_i} defines the expected power value of a wind farm for all wind speeds u in one wind direction α_i which is given by

$$\begin{aligned}
 P_{\alpha_i} &:= E[P_{\alpha_i}(u)] \\
 &= \int_0^\infty P_{\alpha_i}(u) \cdot f_{\alpha_i}(u) du \\
 &= \int_{u_{\text{cutin}}}^{u_{\text{cutout}}} P_{\alpha_i}(u) \cdot f_{\alpha_i}(u) du \\
 &\approx \sum_{j=1}^{N_{\text{speeds}}} w_j \cdot P_{\alpha_i}(u_j) \cdot f_{\alpha_i}(u_j)
 \end{aligned} \tag{15}$$

where $f_{\alpha_i}(u_j)$ describes the probability density function of equation (1) of the wind speed distribution for each sector α_i . As defined in section 3.3 u_{cutin} and u_{cutout} are the turbine's cut-in and cut-out speed respectively, w_j is the weight for speed j and

$$P_{\alpha_i}(u) = \sum_{k=1}^{N_{\text{turbines}}} P_{\alpha_i}(u_{\text{inc}_k})$$

denotes the total power output of the wind farm at wind speed u and direction α . $P_{\alpha_i}(u)$ is the power production of one turbine and u_{inc_k} is the incident wind speed at turbine k . Then the incident wind speed is computed by

$$u_{\text{inc}} = (1 - \delta_u)u_0,$$

where u_0 is the unperturbed free stream speed and δ_u is the velocity deficit as defined in section 3.2 at a turbine rotor with perturbed wind inside another turbine's wake.

Finally we define the most important value $\text{AEP}_{\text{gross}}$ for the cost models in section 3.6 with the wind speed distribution described as Weibull distribution $f_{\alpha_i}(u)$ and the power curve $P(u)$ for each wind speed u :

$$\begin{aligned} \text{AEP}_{\text{gross}} &= (8760h + 6h) \cdot P \\ &\approx (8760h + 6h) \cdot \sum_{i=1}^{N_{\text{directions}}} w_{\alpha_i} \cdot \sum_{j=0}^{N_{\text{speeds}}} w_j \cdot f_{\alpha_i}(u_j) \cdot \sum_{k=1}^{N_{\text{turbines}}} P_{\alpha_i}(u_{\text{inc}_{j,k}}), \end{aligned} \quad (16)$$

where P denotes the mean power as defined in equation (14) for a given wind distribution in megawatt (MW). This need to be calculated to the length of one year to get the AEP measured in MWh. Thus we multiply P by $(8760h + 6h)$, where 8760 is the number of hours in one year and the additional six hours in order to take the mean hours per year with consideration of leap years. This results in 365,25 days per year.

3.5 Time-dependent Annual Energy Production

In this section the extension of the AEP calculation as described in section 3.4 will be considered. The extension concerns the wind data, which is in our case the FINO3 data as mentioned in Section 3.1. So far, only the probabilities of wind direction and wind speed with help of the Weibull function are considered. Now, different timeslots are added, so the wind data contain the additional information of hours of the day as subdivided into timeslots such as a twelve hour cycle. So the first slot would be from 0:00 to 12:00 and the second slot from 12:00 to 24:00. Thus for a certain wind directions there are also specially probabilities for the different time-dependent tariffs as shown in Figure 8 and P of Equation 16 changes to

$$P \approx \sum_{t=1}^{N_{\text{timeslots}}} \left(\sum_{i=1}^{N_{\text{directions}_t}} w_{\alpha_i} \cdot \sum_{j=0}^{N_{\text{speeds}_t}} w_j \cdot f_{\alpha_i}(u_j) \cdot \sum_{k=1}^{N_{\text{turbines}}} P_{\alpha_i}(u_{\text{inc}_{j,k}}) \right), \quad (17)$$

where $N_{\text{directions}_t}$ and N_{speeds_t} are the direction and speed probabilities with regard to the timeslot. The individual time-dependent AEP values can also be output individually, without adding them up, so that a time-dependent LCOE and NPV can be calculated in the following section.

This has the advantage of including different tariff cost options for the time-dependent AEP values. The effects will be examined in Section 3.7.

3.6 Cost Model

Based on the $\text{AEP}_{\text{gross}}$ value the different cost models will be introduced in this section. These models evaluate various quantities of interest for a given wind farm and can be used as objective functions for the layout optimization routine [40]. The quantities of interests are the calculated different indicators that point out the economic benefit of a wind farm as represented by Cakar [8]. In the following subsections we consider the net AEP calculation, the leveled cost of energy and finally, the net present value and the internal rate of return.

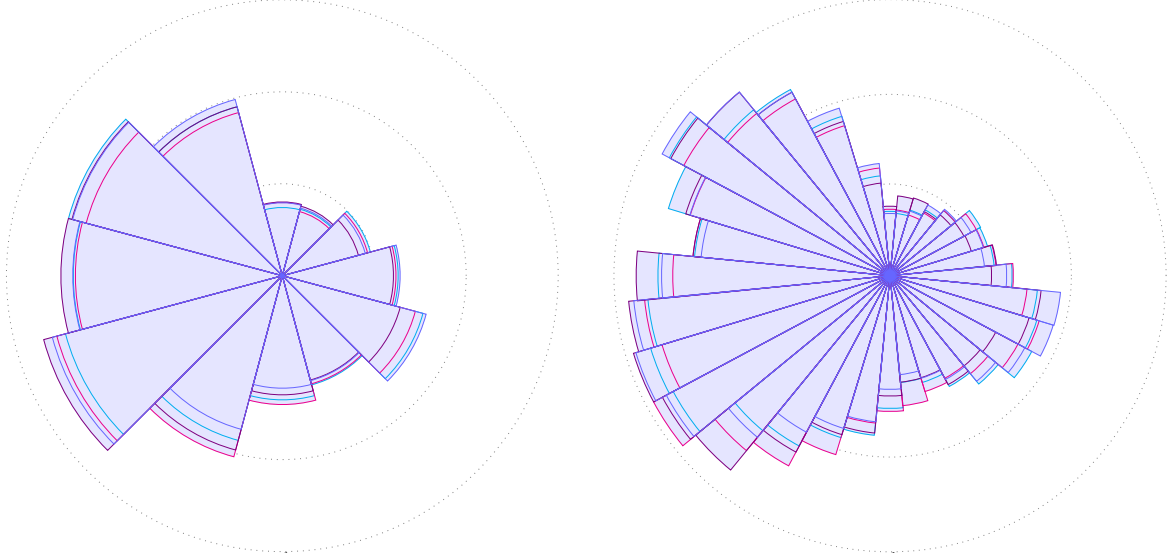


Figure 8: Time-dependent wind direction probabilities. Each color represents a different time interval for the respective wind direction. Clustered probabilities into 12 and 36 direction sectors.

3.6.1 Net Annual Energy Production

So far we computed the gross AEP in equation (16), but this is not quite a realistic measure for wind farm energy production. So, we introduce net AEP by reducing the gross AEP with a constant factor p_{loss} which includes availability losses as a result of turbine and grid downtime of the wind farm. The plant performance lost p_{loss} is the summarized electrical efficiency due to line losses and curtailment. This results in the calculation for net AEP as

$$\text{AEP}_{\text{net}} = \text{AEP}_{\text{gross}} \cdot (1 - p_{\text{loss}}). \quad (18)$$

3.6.2 Levelized Cost of Electricity

To represent the price of electricity per kWh over the whole lifetime of a wind park we introduce the levelized cost of energy (LCOE). This also includes the initial costs and costs of operation. Our cost model uses the formula of the LCOE by Lackner and Elkintion [26] defined as

$$K_{\text{LCOE}} = \frac{C_{\text{capital}} \cdot \frac{(1 + r_{\text{rate}})^\ell \cdot r_{\text{rate}}}{(1 + r_{\text{rate}})^\ell - 1} + C_{\text{o\&m}}}{\text{AEP}_{\text{net}}}, \quad (19)$$

where C_{capital} is representing the total capital costs for turbines, cabling, substation, decommission and other. $C_{\text{o\&m}}$ are the annual costs of operation and maintenance, and discount rate r_{rate} including debt, taxes and insurance over the lifetime of ℓ years.

For the time-dependent LCOE, the equation changes as follows:

$$\text{LCOE}_{\text{tariff}} = \frac{C_{\text{capital}} \cdot \frac{(1 + r_{\text{rate}})^\ell \cdot r_{\text{rate}}}{(1 + r_{\text{rate}})^\ell - 1} + C_{\text{o\&m}}}{\sum_{t=1}^{N_{\text{timeslots}}} \text{AEP}_{\text{net}_t}}, \quad (20)$$

For the future optimization of the costs by means of LCOE, it should be mentioned that the capital costs consist primarily of the material costs for the construction of a wind farm. In addition to the steel for the wind turbines, these material costs also include the cable costs that connect the individual wind turbines. As a result, the total capital costs also depend on the length of the cables laid.

3.6.3 Net Present Value

The net present value (NPV) is an indicator for the actual financial value of a project introduced by Gonzales [18]. It specifies the difference between the current cash inflows and outflows of the project. Thus the higher the value the better is the project. For the full validity of this value it needs to be compared with another project or alternative setting of the considered project. The NPV is defined as

$$C_{\text{NPV}} = C_{\text{PRV}} - C_{\text{capital}} + \sum_{t=1}^{\ell} \frac{\text{AEP}_{\text{net}} \cdot K_{\text{energy}} - C_{\text{o\&m}}}{(1 + r_{\text{rate}})^t}, \quad (21)$$

where the parameter C_{PRV} is the present residual value of the wind farm after the lifetime ℓ in years. Similar to the LCOE C_{capital} includes the total capital costs for turbines, cabling, substation, decommission and other and $C_{\text{o\&m}}$ are the annual operation and maintenance costs with respect to the discount rate r_{rate} . K_{energy} translates the actual price of energy on the market. Usually AEP_{net} , K_{energy} and $C_{\text{o\&m}}$ are time-dependent, but because we are working with averaged values (e.g. the wind data is aggregated from several years), we assume them to be constant in time.

For the time-dependent NPV, instead of a single average energy price, more exact prices are used depending on the time of day, e.g. energy in the evening is worth more than during the day. This makes the result more accurate and the equation changes to:

$$\text{NPV}_{\text{tariff}} = C_{\text{PRV}} - C_{\text{capital}} + \sum_{t=1}^{\ell} \frac{\sum_{t=1}^{N_{\text{timeslots}}} (\text{AEP}_{\text{net}_t} \cdot K_{\text{energy}_t}) - C_{\text{o\&m}}}{(1 + r_{\text{rate}})^t}, \quad (22)$$

3.6.4 Internal Rate of Return

The internal rate of return (IRR) as r_{IRR} is similar to the NPV a measure for the profitability of an investment of a project. r_{IRR} is defined to be the value of r_{rate} in Equation (21) which results in a NPV of zero.

$$C_{\text{NPV}} = C_{\text{PRV}} - C_{\text{capital}} + \sum_{t=1}^{\ell} \frac{\text{AEP}_{\text{net}} \cdot K_{\text{energy}} - C_{\text{o\&m}}}{(1 + r_{\text{IRR}})^t} \stackrel{!}{=} 0 \quad (23)$$

General settings		
Settings	Field size ($x = y$)	Number turbines
Horns Rev 1	1800	15
Tariff settings		
Tariff 1	24h cycle	11 cent
Tariff 2	6h cycle	[14, 4, 6, 20] cent

Table 1: Settings for time-dependent tariff example in Figure 9.

To reach a profitable project, the r_{IRR} should be greater than the real discount rate r_{rate} and any additional risk deficits combined.

3.7 Tariff Consideration

As an example of the usefulness and influence of different tariffs, a square field with 15 turbines is created. The exact settings can be seen in Table 1. The general settings are taken from the wind farm Horns Rev 1 and adapted, as well as the turbine type. With these settings two optimizations are started, first with only one tariff over 24 hours, the other with a 6 hour cycle. It is noticeable that the six-hour interval in the evening has a considerably higher energy price. The basic Local Search algorithm is used as optimizer, which terminates when no improvement can be achieved, as explained later in Section 7.2.1. As optimization goal the NPV value is used, since this includes the energy price. The resulting turbine positions are summarized in Figure 9.

It is noticeable that some turbines are in the same position after both optimizations, while others differ. However, the largest difference between two turbines is 24 meters. Thus it is demonstrated that it makes a distinction whether different tariffs are included or not.

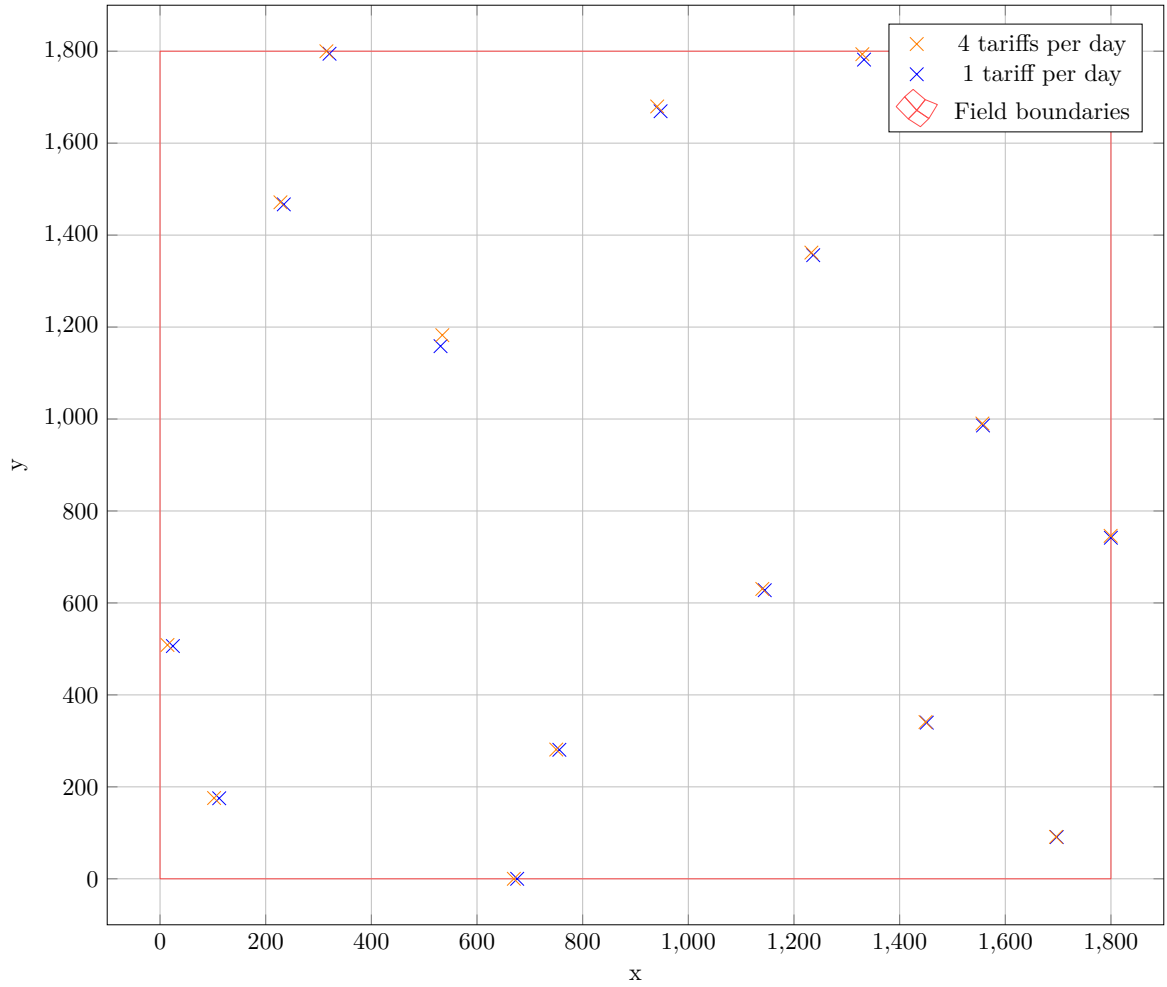


Figure 9: Example for different turbine layouts by one or four tariffs as defined in Table 1. Blue shows the optimized layout with one average tariff and red with four accurate tariffs.

4 AEP of Raw Data

This section introduces a new method for calculating the AEP value. It is based on the idea of using the raw FINO3 data of size N_{rawData} for the calculation because these are the most accurate values we have. The datasets introduced in Section 3 is aggregated data to save computing time. But this aggregation by using a Weibull distribution curve causes some inaccuracies. The Weibull function is only an approximation to the real probabilities of wind speeds as shown in Figure 10.

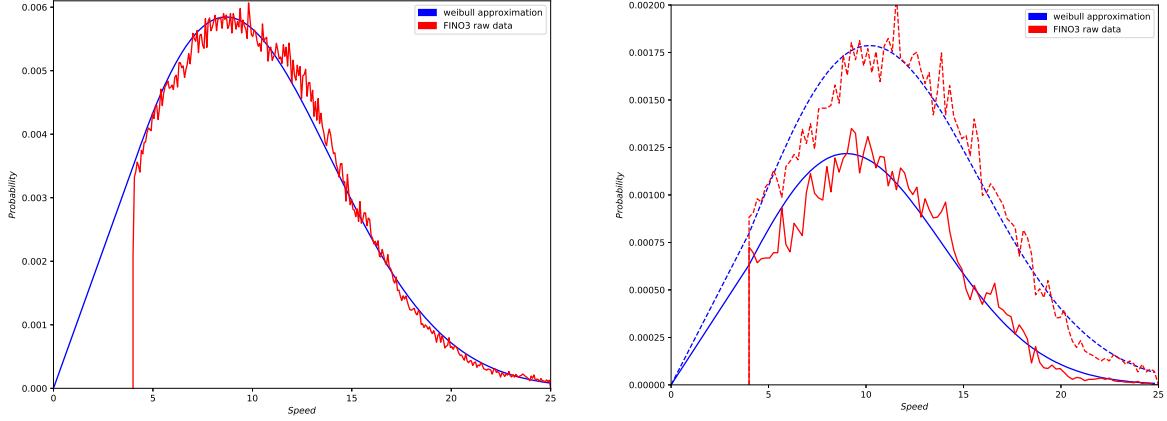


Figure 10: Weibull approximation (blue) in comparison to original FINO3 data (red) in the relevant area of minimum 4 m/s to maximum 25 m/s. On the left hand side for all directions at once and on the right hand side for two wind directions out of 12 for the wind direction at 90 degrees (straight line) and at 210 degrees (dotted line).

The original FINO3 data set has nearly 300000 data pairs, which is too much to simulate each with their wind direction and speed.

Therefore firstly some fixed discretization for wind direction and wind speed are simulated, so that a grid is created. From this we can quickly determine the power values for the direction and speed of the individual FINO3 raw data. The underlying grid is more accurate depending on the number of simulated wind directions and speeds as shown in Figure 11 as heat map. Every grid cell represents the power outcome of one specific simulated wind direction and speed. By examine the graphic for Horns Rev 1 stands out that on specific wind directions the power outcome becomes more or less strong, that is because of the wake effect has more impact in some directions.

So for one specific wind speed, the power outcome reaches its peak for every direction. However, it becomes visible what a large influence the discretization of wind direction and speed has. Without the exact direction resolution we would not have an exact computation on the stronger wind directions.

Besides the power outcome we also need the raw wind data to be classified into the same resolution. Thus we have the number of wind data sets which occur with a

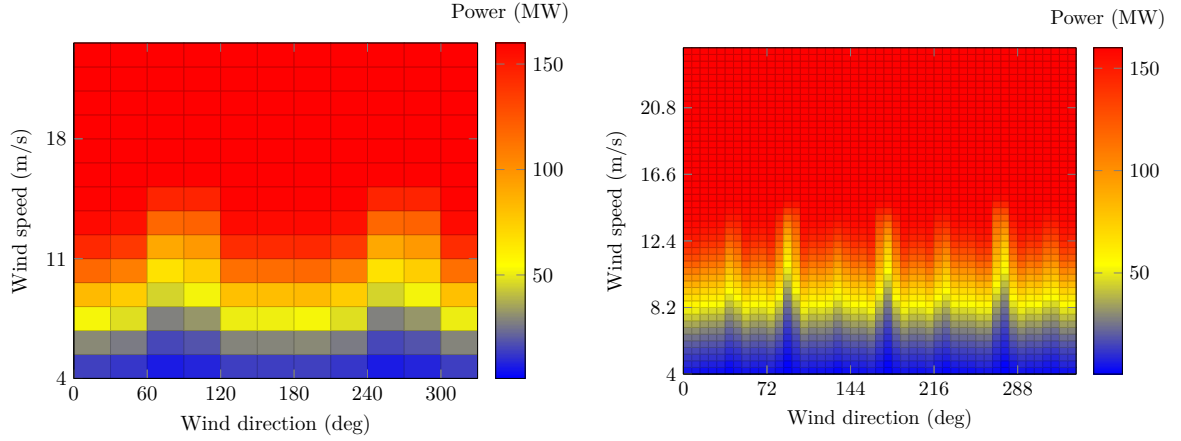


Figure 11: Heat map of simulated AEP output grid for every wind direction and speed pair of the Horns Rev 1 wind farm. On the left side with a coarse resolution of 12 directions and 15 speeds. In contrast to a high resolution with 48 directions and 50 speeds on the right side. The main difference can be seen in the fact that at high resolution individual wind directions with little power output are clearly recognizable.

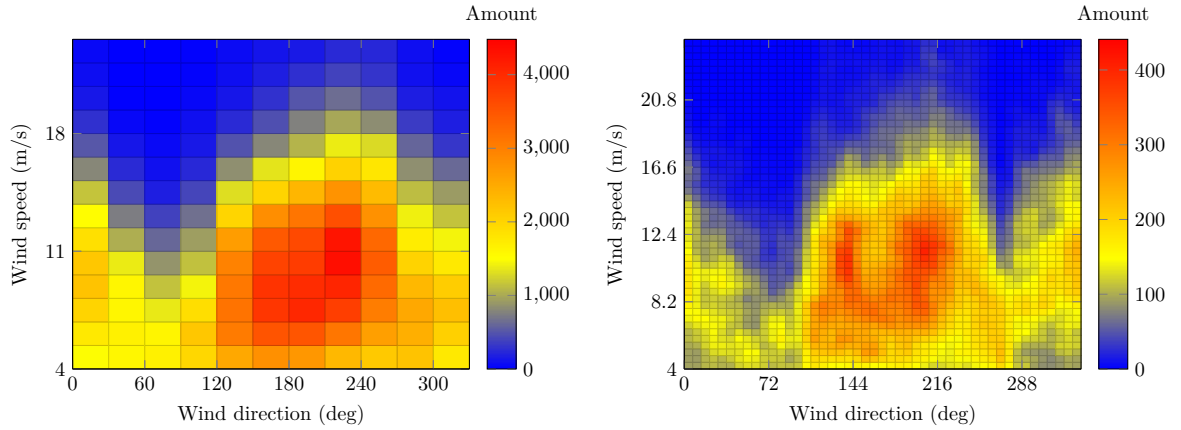


Figure 12: Number of raw data pairs from FINO3 measurement at every wind direction and speed visualized as heat map. On the left side with a discretization of 12 directions and 15 speed subdivisions and on the right side with a higher resolution of 48 directions and 50 speed subdivisions. In both figures a very clear main wind direction becomes visible.

specific direction and speed, as shown in Figure 12. From these the probabilities can be calculated by dividing by the total number of wind data. By investigating Figure 12 it becomes visible from which direction and at which speed the wind arrives most frequently.

To calculate the overall AEP we need to combine the two information sets of simulated wind park power and probability of the occurrence of wind from each direction and speed. To assign the combined power from this grids there are two different options, the nearest neighbour and the bilinear interpolation. P of equation (16) changes to

$$P_{\text{interpolation}} \approx \frac{1}{N_{\text{rawData}}} \cdot \sum_{i=1}^{N_{\text{rawData}}} P_{\text{interpolation}(\text{dir}, r_i)}(\text{interpolation}(\text{spd}, r_i)), \quad (24)$$

where N_{rawData} defines the number of direction speed pairs in the raw data set which are not invalid. $\text{interpolation}()$ calculates the interpolation method as described below with all directions/speeds and actual raw data direction/speed as input.

4.0.1 Nearest Neighbour Interpolation

The Nearest Neighbour (NN) interpolation [4] is a simple method of multivariate interpolation useful for our two dimensional case. The NN algorithm selects briefly the value of the nearest point with the shortest distance between that points and does not consider any other point.

In our case, for a given wind speed and direction from the raw data set the power needs to be approximated by the simulated points. Finally all wind elements of the raw data set with corresponding power values of the simulation have to be added.

The combined values for every grid cell with the NN algorithm for the Horns Rev 1 wind park and FINO3 wind set is shown in Figure 13 for a weak and strong resolution. As shown in Figure 13, this grid combines the strong cells of the simulation outcome and frequency of certain wind pairs. The advantage of this simple NN algorithm is that it is computational very fast.

4.0.2 Bilinear Interpolation

The Bilinear Interpolation [4] is an advanced interpolation method which is an extension of linear interpolation. This method requires a rectilinear 2D grid which is a tessellation by rectangles or parallelepipeds that are not, in general, all congruent to each other. This criterion is fulfilled by our two given grids, since they all consist of square cells as shown above. The key idea of Bilinear Interpolation is to perform linear interpolation first in one direction and then again in the other direction. Although each step is linear in the sampled values and in the position.

In other words our unknown wind data point calculates a bilinear interpolation with the four surrounding simulated power points. With all directions/speeds and actual raw data direction/speed as input. The results of the Bilinear Interpolation are shown

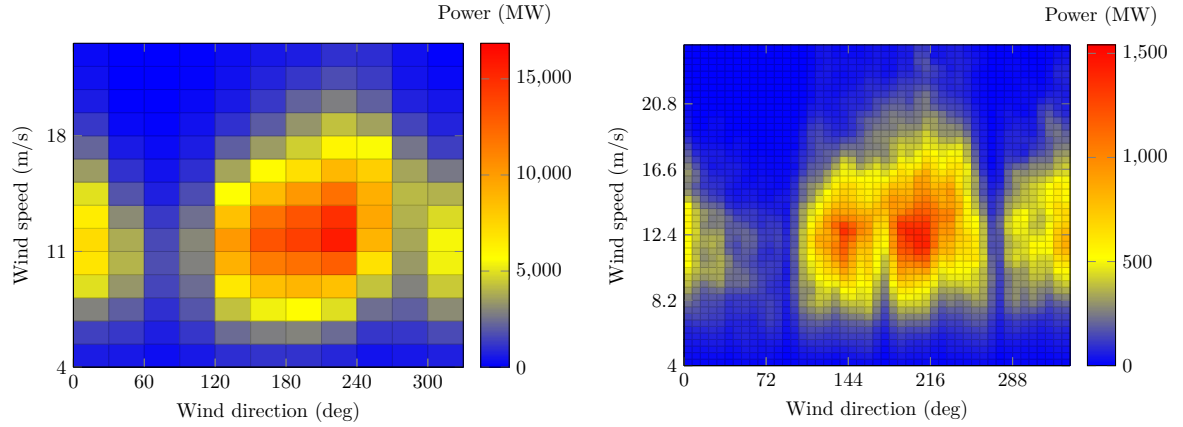


Figure 13: Nearest Neighbour combination of the simulated power grid of Figure 11 and the occurrences of wind direction speed pairs of Figure 12. Results in the final power occurrence of each grid cell. The sum of these individual grid cells results in the simulated AEP value of a wind farm.

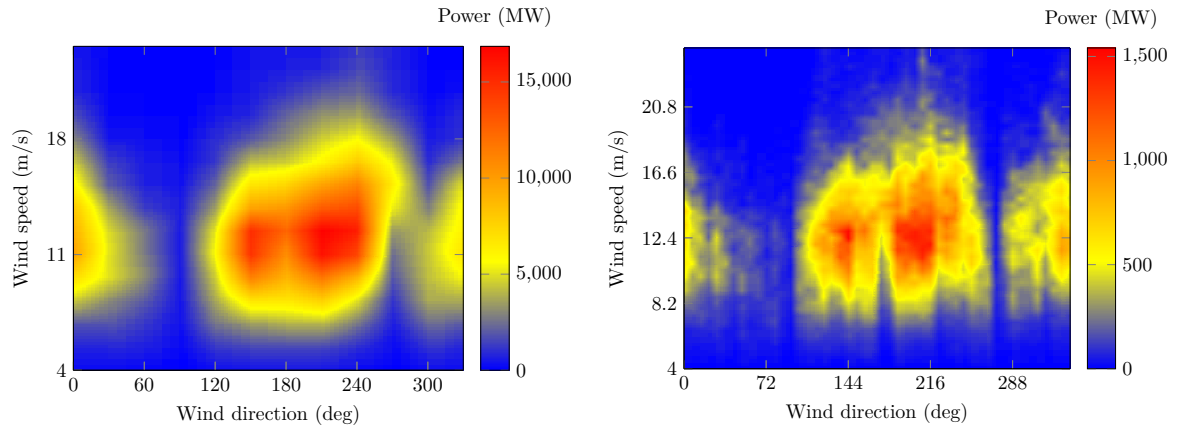


Figure 14: Similar combination of the simulated power and wind data pair occurrences as in Figure 13. However, Bilinear Interpolation is applied so that the individual grid cells merge into each other. Also for coarse and high resolution.

in Figure 14 which in the end have to be summed up. It becomes visible that in contrast to the NN method, the boundaries between the grid cells become blurred. However, with both approaches it is noticeable that a too low resolution leads to a coarse and altered appearance which then may no longer correspond to reality. An investigation of this resolution follows below.

4.1 Results

For an investigation of the two raw data approaches the wind farm Horns Rev 1 and the FINO3 wind data were used. The underlying wind data set for the standard calculation corresponds to the Weibull model with 12 wind directions. First the wind speed resolution will be considered. The value is specified as interval size starting by 2.0 up to a resolution of 0.01. A value of 1.0 corresponds to an interval of 1 m/s. The quantity of simulated wind directions is made dependent on this value. Whereby the Horns Rev 1 turbines with cut in speed of 4 and cut out speed of 25 results in a corresponding size of 21 simulated wind speeds. The results of this investigation with a constant wind direction number of 36 is shown in Figure 15. It stands out that the simulated AEP power outcome changes only slightly with increasing resolution and the resulting values become slightly less for all three approaches, so the differences do not become larger between the individual methods. In summary, we can conclude that the resolution of the wind speed has only a small effect on the accuracy of our simulated results and can therefore be neglected in later optimization to achieve a good run time.

For an consideration of the wind direction resolution the same underlying data is used as above. The number of wind directions directly indicates how many wind directions are simulated. For example, a number of 36 means that every 10th wind direction is simulated. The examined number corresponds here from 6 to 720 directions and a constant wind speed resolution of 1.0. The results of this investigation for all three approaches can be viewed in Figure 16. It quickly becomes apparent that the resulting graph is not as uniform as at wind speeds. This can be briefly explained by the fact that the simulated wake effect is stronger or weaker depending on whether the selected directions are good for the wind farm or not. Basically, we can say that the strong fluctuations in the first part of the graph are caused by too few simulated wind directions. What follows is that the few individual wind directions have a very strong influence on the overall result.

From a number of 30 directions it is noticeable that the normal AEP calculation and NN slowly settle to one value and remain constantly close to each other over the entire evaluated range. This can be explained by the fact that the calculations are actually very similar to each other, since the 12 wind directions with Weibull are only a summary of the FINO3 data and have small inaccuracies as mentioned at the beginning of this section. However, this is interpolated and scaled by the OpenWind validated calculation, whereby according to our results the overall probabilities decrease slightly. Finally only the bilinear interpolation has even greater fluctuations in the following. This could be explained by the fact that many wind data pairs lie at the edge of

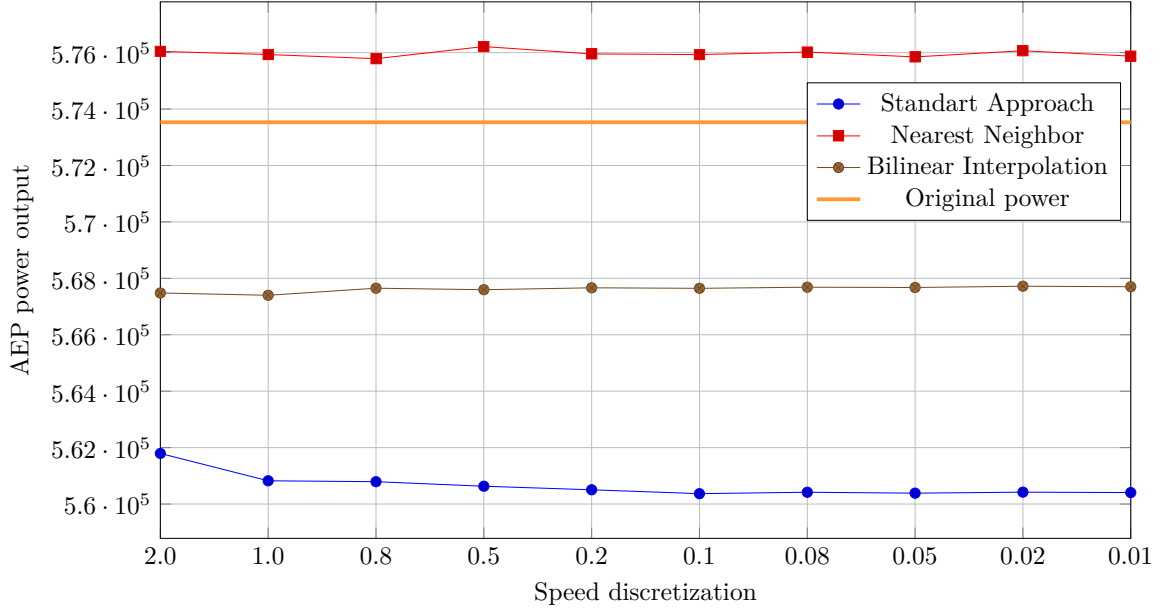


Figure 15: Investigation of wind speed resolution with a constant number of 48 wind directions. This illustrates that a higher speed resolution has almost no effect on the results. To compare the two approaches, which are examined in this thesis, the standard approach and the original AEP value are still available. This results from the simulation of all 300,000 FINO data.

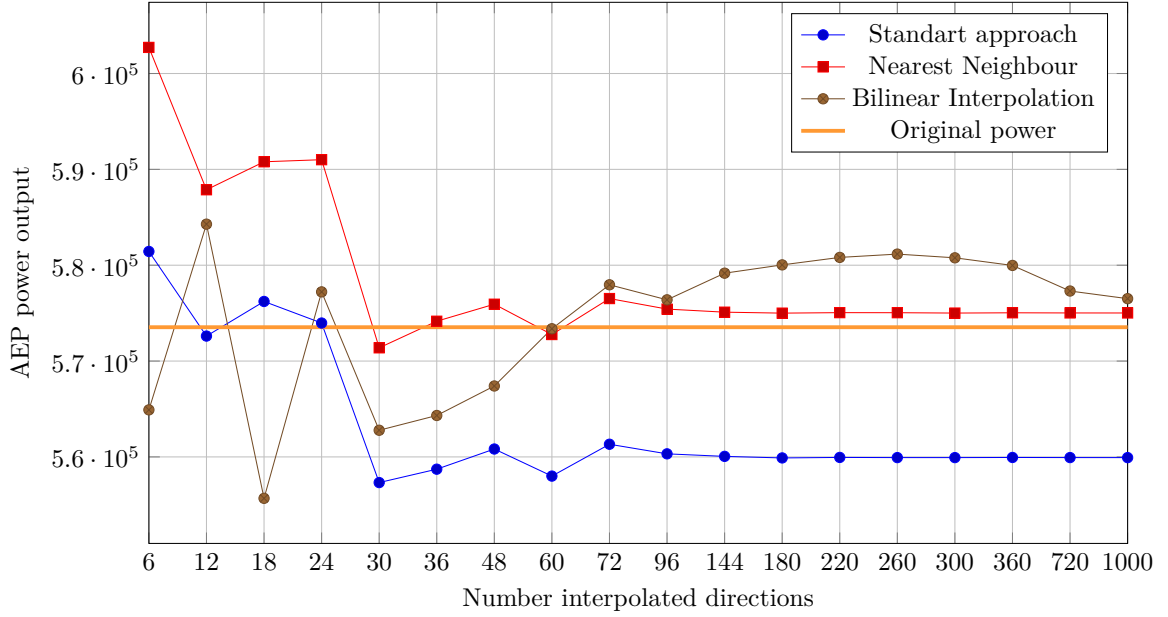


Figure 16: Evaluation of wind direction resolution with a constant wind speed interval of 1.0. It becomes clear that the wind direction resolution has a significant influence on the result and converges at a very high resolution to the original AEP value.

the strong power areas which have been identified above and evaluated by Bilinear Interpolation larger values than the other two methods. Consequently, the general power outcome grows to a maximum at 260 wind directions and then slowly returns to normal.

In summary, we can conclude that the resolution of wind speeds can be neglected, but great attention should be paid to the number of simulated wind directions. Overall, we would recommend a minimum number of 36 wind directions to have comparable results for optimization.

5 Wind Farm Modelling with Uncertainties

In this section we will explain the fundamental characteristics of uncertainties based on the works of Richter [34] and Cakar [8]. In this process the parameters of our simulation presented in Section 3 are not be deterministic any more. One way to take into account these uncertainties is to use the theory of probability, to describe the uncertain parameters as random variables or random processes. These so called uncertain parameters are perturbed by a Gaussian normal distribution to reach a stochastic model [39].

5.1 Uncertain parameters

As described in Section 3 we have several input parameters which will modeled as random variables ξ to consider the uncertain disturbance. The normally distributed variables are centered around the original undisturbed value. This can be delineated to a multiplication between the undisturbed value and a normal distribution $\mathcal{N}(1, \sigma)$. Following uncertain parameters are examined in this work:

Uncertain parameters	Influencing factors
1 Wind speed ξ_{wind}	Inaccurate measurements, future variability.
2 Wake Effect ξ_{wake} C_t Curve ξ_{ct} Surface roughness ξ_{rough}	Model inaccuracies. Atmospheric stability. Surface condition changes.
3 Power Curve ξ_{power}	Impacts of atmospheric stability.
4 Plant performance losses $\xi_{\text{performance}}$ Capital costs ξ_{capital} Annual O&M costs $\xi_{\text{o\&m}}$ Discount rate ξ_{rate} Energy price on market ξ_{energy}	Electrical efficiency and weather effects. Fluctuating material prices. Technology standards. Economical fluctuations. Changing market prices.

Table 2: Ten uncertain input parameter which will be perturbed by a random variable ξ of its corresponding normal distribution $\mathcal{N}(\mu, \sigma)$ and their influencing factors. The parameter σ is obtained by the max deviation value d . This value indicates that in the worst case the input parameter values will be perturbed by $\pm d\%$ which is achieved with the right determination of the normal distribution.

5.2 Stochastic Model

These uncertain parameters are now included into our simulation model of Section 3.

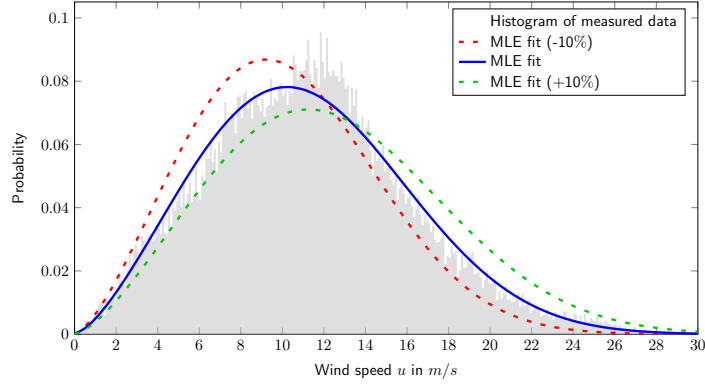


Figure 17: Fitted Weibull distribution with maximum likelihood estimation (MLE) for wind speed distribution over seven years for one wind direction sector $\alpha_i \in [225^\circ - 255^\circ]$ measured at the FINO3 research platform mentioned in Section 3.1. Red and green plots representing the fitted weibull distribution with MLE after perturbing the wind speed data with a factor of $\pm 10\%$. The random variable $\xi_{wind}(u)$ describes the weibull distribution between the highest red plot and the lowest green plot with a probability of 99.73%. Source: Richter [34]

5.2.1 Uncertain Wind Model

Due to inaccurate measurements, future variability and further interferences [14] the distribution of wind speed u is an uncertain parameter with strong influence. For this purpose we perturb the raw wind data set explained in Section 3 of the wind speed by a normally distributed random variable ξ_{wind} . So that perturbed probability density functions of the weibull distribution are archived as shown in Figure 17. Cakar [8] and Tuzuner [41] have shown that a disturbance d of the wind speed corresponds to the perturbation d of the weibull parameter λ . This allows us to formulate the resulting probability for each wind speed u of equation 1 as random variable:

$$\tilde{f}_{\alpha_i}(u, \xi_{wind}) = \left(\frac{k}{\lambda \cdot \xi_{wind}} \right) \cdot \left(\frac{u}{\lambda \cdot \xi_{wind}} \right)^{k-1} \cdot \exp \left(- (u \cdot \lambda \cdot \xi_{wind})^k \right) \quad (25)$$

where $k > 0$ is the shape parameter and $\lambda > 0$ is the scale parameter of the Weibull distribution.

5.2.2 Uncertain Wake Model

The wake effect prediction is perturbed due to different model input inaccuracies and uncertainties. So we need to include uncertainty concerning any proposed neighbouring sites [14]. To process this effect we perturb the velocity deficit of a wake with a normally distributed random variable ξ_{wake} . Furthermore the wake model depends on the surface roughness z_0 and the C_t curve. Due to inaccuracy measurements and atmospheric stability, we also perturb this parameter with a normally distributed random variable

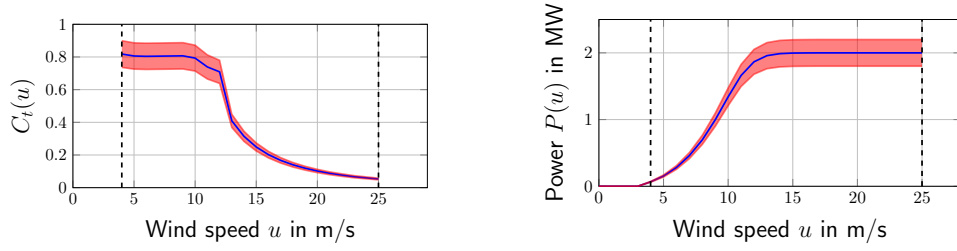


Figure 18: Perturbed C_t and power curve of the turbine Vestas V80. In the relevant range of cut-in speed of 4 m/s and cut-out speed of 25 m/s (dashed vertical lines). The red tube represents the C_t and power curve with a perturbation of $\pm 10\%$. Source: Richter [34]

ξ_{ct} as shown in Figure 18. The value of $C_t(u_0) \cdot \xi_{ct}$ must not be greater or equal to one, as based on equation (26). The surface roughness depends on the topography and flora as mentioned in Section 3 [42]. It follows from this that also the parameter z_0 has to be stochastic and will be perturbed with a normally distributed random variable ξ_{rough} . Summarized the velocity deficit behind a turbine at any point x from equation (8) is modified to

$$\widetilde{\delta}_u(x) = \frac{1 - \sqrt{1 - C_t(u_0) \cdot \xi_{ct}}}{\left(1 + \frac{x}{D \cdot \ln(z/z_0 \cdot \xi_{rough})}\right)^2} \cdot \xi_{wake}. \quad (26)$$

5.2.3 Uncertain Power Generation

The turbine performance is perturbed due to material fatigue which leads to inaccuracy in the power curve. In addition there is an uncertainty on the performance under site conditions for which the power curve might not be valid. There are also other inaccuracies and losses as the impact of atmospheric stability, uncertainty associated with icing losses and other environmental losses which need to be included. Summarized we perturb the power curve by a normally distributed random variable ξ_{power} as shown in Figure 18. This effect results in

$$\tilde{P}(u, \xi_{power}) = P(u) \cdot \xi_{power}. \quad (27)$$

5.2.4 Uncertain Gross Annual Energy Production

The uncertain gross AEP consists of the probability density function (25) for the uncertain wind distribution, the uncertain velocity deficit function (26) and the uncertain power function (27). It changes equation (16) to:

$$\begin{aligned} \tilde{E}_{AEP_{gross}} \approx & (8766h) \cdot \sum_{i=1}^{N_{directions}} w_{\alpha_i} \cdot \sum_{j=0}^{N_{speeds}} w_j \cdot \tilde{f}_{\alpha_i}(u_j, \xi_{wind}) \\ & \cdot \sum_{k=1}^{N_{turbines}} \tilde{P}_{\alpha_i}(u_{inc_{j,k}}, \xi_{power}, \xi_{ct}, \xi_{rough}, \xi_{wake}) \end{aligned} \quad (28)$$

5.2.5 Uncertain Net Annual Energy Production

Similar as for the gross AEP the net AEP changes to the uncertain net AEP by depending on availability losses p_{loss} which consider the grid and turbine downtime. Since these influences depend on outer circumstances this parameter should also be modeled stochastic. So, we perturb the availability losses (18) with a normally distributed random variable $\xi_{\text{performance}}$ such that the net AEP changes to:

$$\tilde{E}_{\text{AEPnet}} = \tilde{E}_{\text{AEPgross}} \cdot (1 - p_{\text{loss}} \cdot \xi_{\text{performance}}). \quad (29)$$

5.2.6 Uncertain Levelized Cost of electricity

The capital costs C_{capital} mainly depend on the price of steel and cable. Since the long planning stage of several years for a wind farm the calculation depends on long-term predictions for those prices which is very volatile. The same applies for the discount rate r_{rate} which is in an early planning stage very unsure and the price of steel based annual operation and maintenance $C_{\text{o\&m}}$. Thus we perturb these with normally distributed random variables ξ_{capital} , ξ_{rate} and $\xi_{\text{o\&m}}$. Summarized these parameters form the levelized cost of energy 19 as follows:

$$\tilde{K}_{\text{LCOE}} = \frac{C_{\text{capital}} \cdot \xi_{\text{capital}} \cdot \frac{(1 + \tilde{r}_{\text{rate}})^\ell \cdot \tilde{r}_{\text{rate}}}{(1 + \tilde{r}_{\text{rate}})^\ell - 1} + C_{\text{o\&m}} \cdot \xi_{\text{o\&m}}}{\tilde{E}_{\text{AEPnet}}}, \quad (30)$$

where \tilde{r}_{rate} is the perturbed discount rate which is valid $\tilde{r}_{\text{rate}} = r_{\text{rate}} \cdot \xi_{\text{rate}}$.

5.2.7 Uncertain Net Present Value

The net present value (21) mainly depends on the price of energy per kWh K_{energy} which is defined in many countries by political laws. Thus this value is unsure in an early planning stage and is perturbed with a normally distributed random variable ξ_{energy} . This changes the equation of NPV used so far to

$$\tilde{C}_{\text{NPV}} = C_{\text{PRV}} - C_{\text{capital}} \cdot \xi_{\text{capital}} + \sum_{t=1}^{\ell} \frac{\tilde{E}_{\text{AEPnet}} \cdot K_{\text{energy}} \cdot \xi_{\text{energy}} - C_{\text{o\&m}} \cdot \xi_{\text{o\&m}}}{(1 + \tilde{r}_{\text{rate}})^t}. \quad (31)$$

5.2.8 Uncertain Internal Rate of Return

As in Section 3.6.4 the uncertain internal rate of return \tilde{r}_{IRR} is the discount rate r which makes the uncertain net present value of (31) equal to zero. For a profitable project this value should be greater than the discount rate r_{rate} plus risk deficits.

6 Multilevel-Monte Carlo Methods

In the area of UQ we want to determine quantitative characterization and reduction of uncertainties, or also fundamentally how large the influence of such uncertainties is in the simulation of wind farms. An attempt is made to determine how likely certain results are if some aspects of the system are not precisely known. To do this, the model was changed in Section 5 so that a random variable can be used to influence the simulation. Consequently, values in our model can be disturbed by random variables. So, to compute the propagation of uncertainties of the random parameters through the model, we need the different so-called Monte Carlo methods. This technique generates several realizations, named samples, of the random parameters according to their distributions.

In this section the Multilevel-Monte Carlo (MLMC) and the advanced quasi-MLMC method from the field of Uncertain Quantification (UQ) are introduced. To do this, we consider the fundamental techniques of the classical Monte Carlo method and the random variable generation based on Richter [34] and Cakar [8] first. The approaches has the advantage to delimit risks beforehand in order to prevent losses because of misconceptions or other sources as mentioned before [21].

By using these methods, we can investigate the influence of individual uncertainties in input parameters, as mentioned in Section 5, onto the model outputs. Therefore, we introduce methods which allow us to quantify the input parameter influence on a certain quantity of interest. For this purpose a combination of probability theory and statistical practice is used. This mathematical models represent scenarios from the real world and investigates uncertainties for those simulation inputs.

To investigate the influence of uncertain parameters on the input parameters of the different models, we have to perturb them like explained in Section 5 with use of different sampling methods. Then we use this perturbed parameters in our simulation model to get an individual outcome. With help of the law of large numbers and the central limit theorem we can predict an overall estimated outcome. To realize this sampling methods are necessary which calculate random variables from probability distributions to perturb the input parameter. For this purpose every input parameter has its own specific distribution as defined before. It is important to note that the size of samples highly affect the accuracy of the results so that with a larger number of samples more accurate results will be computed. In contrast to the classic Monte Carlo methods, the MLMC approaches in particular try to find this ideal number of samples for a sufficiently good result.

6.1 Monte Carlo

The classical Monte Carlo (MC) sampling method is simplified the repetition of random sampling and statistical analysis of the outcomes [33]. This sampling method generates random values with help of a random number generator and transforms them to random variables of a probability distribution to perform the perturbation. By this perturbation in every sample step we get the input parameters according to

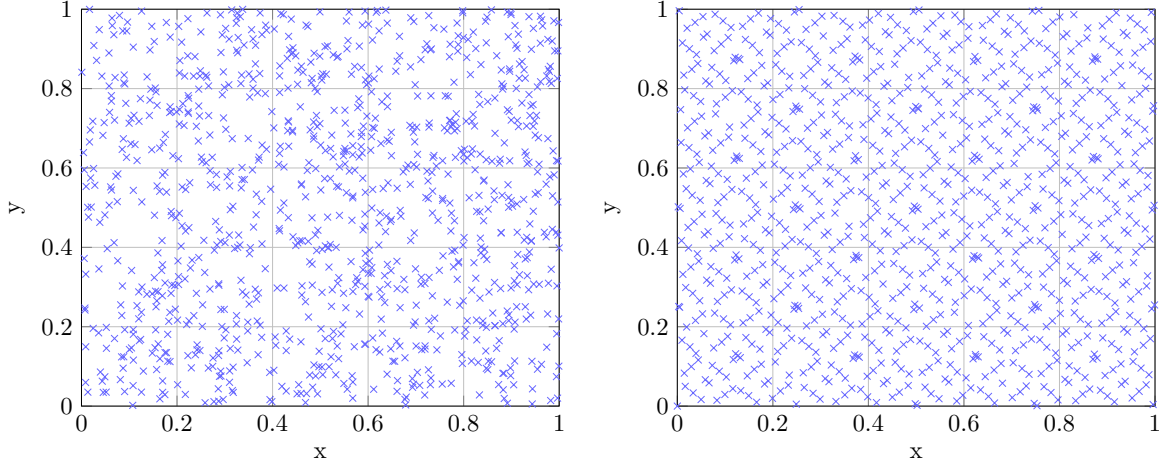


Figure 19: Random number (left) and Sobol generator (right) on a 2D graph with 1000 samples. The normal random number generator creates larger gaps between the samples, whereas the Sobol generator produces equally distributed samples. Source: Cakar [8]

their specific distributions. After repeating this procedure for a sufficient number of samples the resulting distribution can be analysed. For our purpose the mean value has the greatest interest defined by

$$\mu = \mathbb{E}[Q_N], \quad (32)$$

where Q_N is the set of results of N samples with perturbed data as described before and

$$\mathbb{E}[Q_N] = \frac{1}{N} \sum_{i=1}^N Q_i. \quad (33)$$

The mean value is also the estimated result of a Monte Carlo run with N samples. In order to define the variance, the standard deviation is needed first.

$$\sigma = \sqrt{\frac{1}{n-1} \sum_{i=1}^n (x_i - \mu)^2} \quad (34)$$

This is a measure for the spread of the entries of the data set. A big value indicates that most of the entries are far away from the mean μ .

The variance σ^2 is the square of the standard deviation σ and states different to the standard deviation not the wideness of the spread but the strength of the spread referred to the data set as defined in the following:

$$\sigma^2 = \frac{1}{n-1} \sum_{i=1}^n (x_i - \mu)^2 \quad (35)$$

If one input parameter is considered it is easy to fill the whole probability space but

for a multidimensional case it is difficult to achieve an even distribution without gaps as shown in Figure 19. Thus an even larger number of samples is required to consider the empty spaces and reach a sufficient accurate estimation value. Nevertheless, with the classic Monte Carlo method, it is not possible to ensure that a sufficient number of samples has been selected. This is due to the fact that the number of samples must be selected each time as an input parameter. Above all, the correct number of samples is not known and is different for each simulation case. This problem is countered by MLMC's approach.

Also the generation of random numbers for this process is a difficult task in practice as computers are deterministic machines. Here we use the pseudo random numbers generator from the C++ standard library.

6.2 Quasi-Monte Carlo

The quasi-Monte Carlo (QMC) sampling method is an improvement of the classical MC method from before. The procedure is similar to the one of MC which generates the random variables with the help of a low discrepancy sequences. These sequence values then will be transformed to random variables of a probability distribution. For the MC method a random number generator produces independent and identically distributed random numbers. The problem of this random number generator as mentioned before is a significant discrepancy of the generated numbers which results in a not evenly distribution. Thus a large number of samples is needed to reach an sufficient result.

For this purpose the quasi-Monte Carlo method uses an approach of Morokoff and Caflisch [28] to reduce the discrepancy of the generated numbers and also reduce the size of samples. The authors investigated different approaches of low discrepancy sequences for this issue. One characteristic of these sequences is that they are infinite. So for every number of samples the generated values of the sequence stays uniformly distributed. Morokoff and Caflisch investigated three different low discrepancy sequences named Halton, Sobel and Faure sequence. It turns out that Halton sequences are the best for up to around six dimensions and for higher dimensions the Sobel sequence generator is better. Thus we consider the Sobel sequence because we want to be able to perturb more than six input parameters.

The Sobel sequence is simplified an infinite sequence of uniformly distributed values in $[0, 1)$ and generates new values by filling the empty spaces, as shown in Figure 19 for the two dimensional case with 1000 points. These points are spread more evenly and with a certain scheme, so that there are less an smaller areas that not filled. In comparison with the classic Monte Carlo random generator the values are significantly better distributed. For detailed explanation of the Sobel generation of the sequences see Bratley and Fox [31].

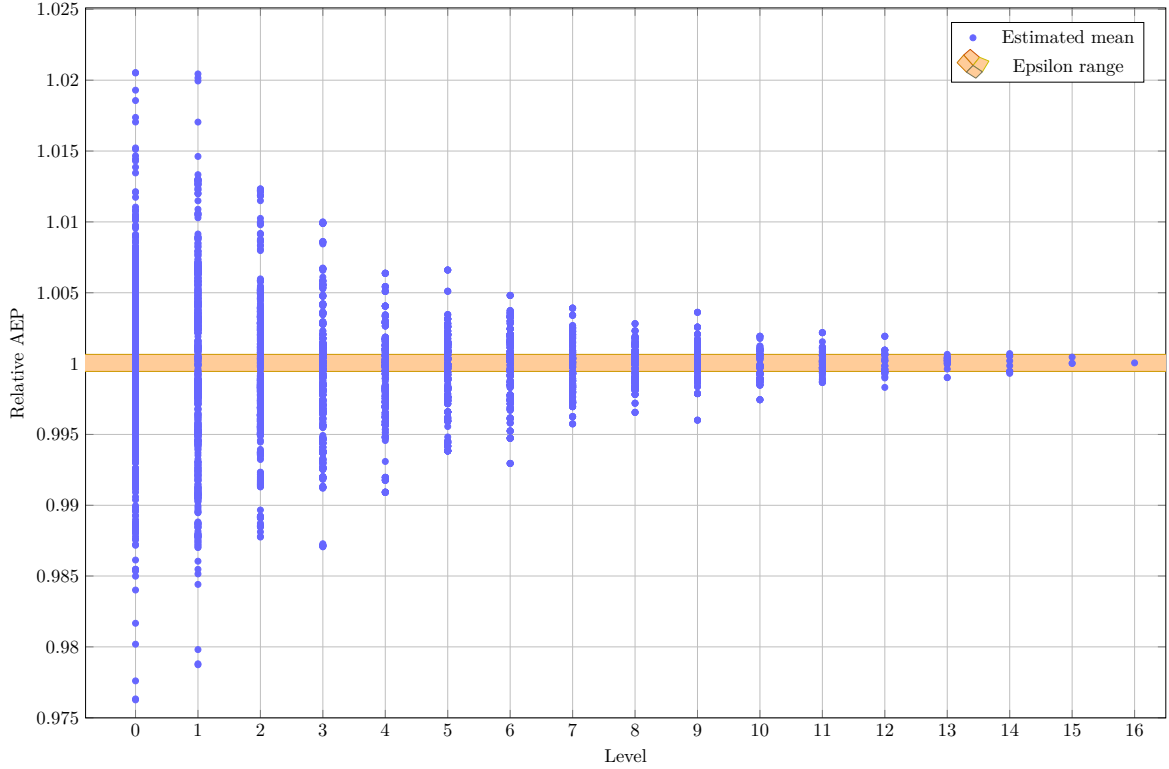


Figure 20: Convergence study of the MLMC method over 100 repetitions and an epsilon value of 0.005%. There is a clear approximation of the relative AEP values to the optimum with rising levels.

6.3 Multilevel-Monte Carlo

The multilevel-Monte Carlo (MLMC) method extends the classical Monte Carlo method on different level with increasing accuracy. The MLMC method used in this thesis based on the work of [17] and Pisaroni [32]. The generation of random values and perturbing the input parameters of the different models works similar to the MC method. As mentioned before the sampling method results in a non-regular distribution which requires a large number of samples. However, this does not verify what a sufficiently large number of samples is to achieve an acceptable estimation.

For this purpose the MLMC method generates a new level of samples when the resulting estimation value is not acceptable. At this new level of samples the accuracy of the set will be increased by increasing the number of samples and also the number of wind directions and wind speeds that are simulated. The samples from the previous level are also included in the newly created set. This results for the mean μ of the specific level L in

$$\mu^L = \mathbb{E}[Q_N^L], \quad (36)$$

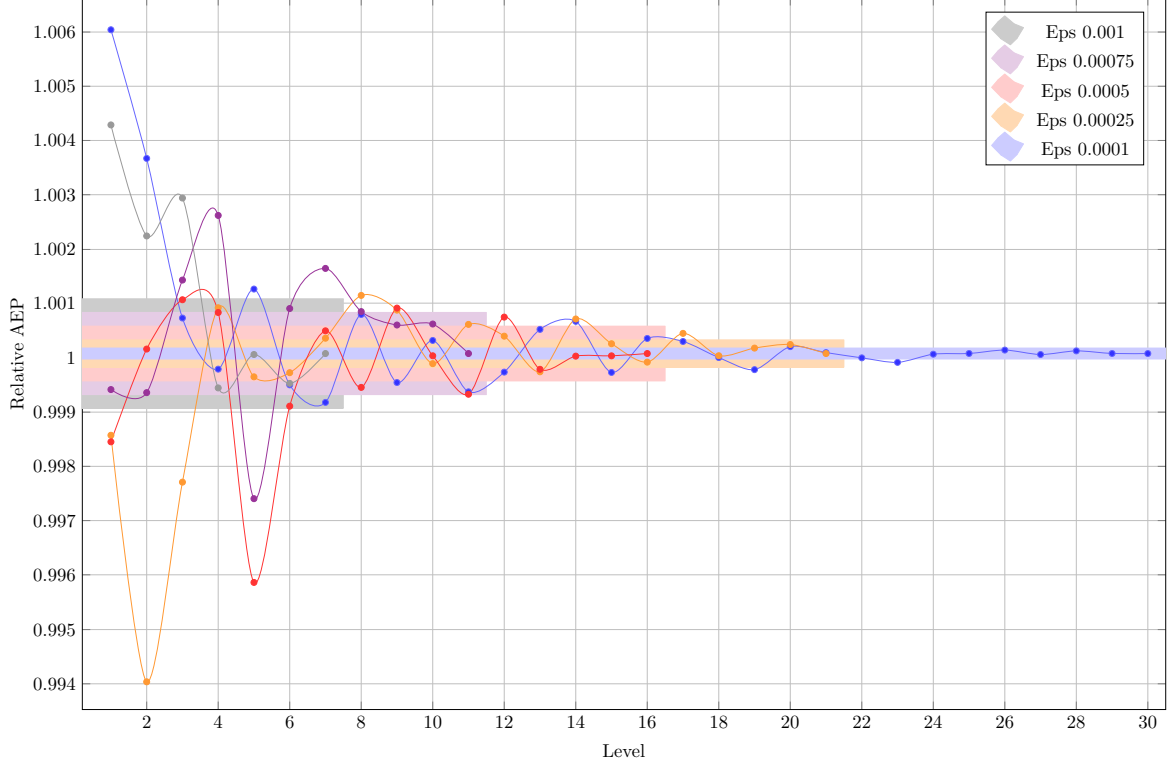


Figure 21: Convergence study of the QMLMC method with different epsilon values. With greater accuracy epsilon, the number of levels also increases to fulfill the criteria.

where Q_N^L is the set of results of N samples of Level L with perturbed parameters and

$$\mathbb{E}[Q_N^L] = \mathbb{E}[Q_{N^0}^0] + \sum_{l=1}^L \mathbb{E}[Q_{N^l}^l - Q_{N^{l-1}}^{l-1}]. \quad (37)$$

Each of the estimations $\mathbb{E}[Q_{N^l}^l - Q_{N^{l-1}}^{l-1}]$ is then approximated by a Monte Carlo method of the specific level. Thus, the results of the previous levels are not lost but are included in the current level.

The criteria for an acceptable estimation result is a convergence criteria which checks the last levels for differences between a certain value ε depending on the normally simulated result. It starts with a fixed number of samples in the first level and increases with each level at a constant growth rate. The algorithm terminates when convergence is reached and the results of the last levels lie within the accuracy criterion epsilon ε . Used the multilevel-Monte Carlo method hundred times on a wind farm, the increasing accuracy with growing level and an estimation value which converges for every run in the orange area of ε , as shown in Figure 20. The strength of the convergence depends on the growth parameters, which increase the accuracy of the samples from level to level. However, the values of the growth parameters are not relevant for the accuracy

of the estimated result, since convergence always takes place. Only the running time varies, depending on whether the selected parameters perform effectively with the accuracy criterion ε .

The advantage of the MLMC method, compared to the previously explained methods, is that it is not necessary to know what a sufficient number of samples is to get a satisfying result. Thus a reusable estimated result is generated for each input parameter.

6.4 Quasi-Multilevel-Monte Carlo

The quasi-Multilevel-Monte Carlo (QMLMC) method is a combination of MLMC and the quasi-MC method. The estimation is achieved over several levels, but instead of a normal random generator, the Sobel generator of QMC is used. The same input parameters for growth and convergence criteria are used as for the MLMC method. A history of estimated results across levels with different ε values can be seen in Figure 21. It is noticeable that with a larger ε value, fewer levels are required to achieve this accuracy.

The advantage here, similar to the MLMC method, is that a converging, sufficient result is achieved faster, because the created samples are better distributed in each level, like at the quasi-MC method. And this works independently of the growth parameters and a certain sample size.

7 Multi-Objective Optimization

The multi-objective (MO) optimization is nowadays one of the most important topics in the field of optimization and has an immense practical importance, since almost all real-world optimization problems, as our wind farm layout turbine positioning, are ideally suited to be modeled using multiple conflicting objectives. Thereby multi-objective optimization is an area of multiple criteria decision making that is concerned with mathematical optimization problems to optimize more than one objective function simultaneously. Before the introduction of multi-objective optimizations such problem were solved by scalarizing multiple objectives into a single objective and then execute an optimization algorithm [10].

The main difference to a single objective problem, in addition to the property of at least two distinct goals instead of one, is that there is not exactly one maximum optimized result rather a rise of trade-off optimal solutions named Pareto-optimal solutions which will be explained in detail further below. To find these sets of optimal solutions is the major difficulty of multi-objective optimizations. Thus, it becomes important to find not just one Pareto-optimal solution but as many of them as possible. Two of these solutions represent a compromise between the objectives, and users will be better able to make a decision when presenting such compromise solutions.

These trade-off solutions can now be examined for several properties. If among all Pareto-optimal solutions some variables assume identical values this development signifies that the solution is an optimal solution. However, if other decision variables have different values, so the solutions is a compromise of their objective values. Further goals of multi-objective optimization are the convergence of the Pareto-optimum which is a continuous front without larger gaps. As well as a broad diversification of the Pareto-optimal solutions. These qualities are discussed in more detail in section 7.2 [13].

The multi-objective Optimizer worked out in this thesis is inspired by the ideas of Rodrigues [36], Bauer [6] and Kwong [25]. In order to present the working method of this algorithm as understandable as possible, we will first explain the different objective functions of which we need at least two in order to be able to perform a multi-objective Optimization. Thereby we pursue several approaches. Next we define the Pareto frontier and the corresponding Pareto optimum. Then we introduce the single-Objective Optimizer which we will use for our multi-objective Optimization. Finally we present some results and the application of our optimizer to the three real wind farms for which we have the related data sets.

7.1 Objective Functions

An objective function is the definition of the goal which an optimizer want to maximize or minimize. We define all functions as maximization problems to guarantee a constant working method in the optimizer. We also measure an object function as a relative value so that the different object functions are easier to compare for the opti-

mizer. In addition, an object function is evaluated as a percentage value so that the different object functions are easier to compare for the optimizer. We have investigated four different object functions in the context of this thesis which are presented in the following. The AEP efficiency, UQ variance, LCOE with cable and noise effect.

7.1.1 Annual Energy Production Efficiency

The most commonly used objective function in the development of wind parks is the resulting energy outcome, which is also the main indicator of the subsequent financial income. As explained in Section 3, this is implemented as AEP output. The AEP is the generated energy with wake effect divided by the power without any wind turbulence, i.e. the theoretical maximum power each turbine could reach at the given wind data, if no other turbine was placed around it.

7.1.2 UQ Variance

The first idea for a second objective function is to include the uncertainty quantification from Section 5. This reduces the variance in the result that we simulate using different Monte Carlo methods. As described before, the variance is an important value to examine a sample set for its scattering measure. So it measures how far a set of perturbed results are spread out from their average value. With a lower variance it could be achieved that the general result of our perturbed simulation is more reliable. In order to obtain comparable variance values for different turbine layouts we use the quasi Monte Carlo method. This method uses, as explained above, an equally distributed random sample set to perturb the input variables. As a result, the variance for a specific position layout does not change during multiple applications and thus remains traceable.

To get a first impression with the handling of variances on different turbine layouts we will create some test cases. It is analysed, what the change of the layout affects the variance and if there is a correlation with the AEP. Since a direct correlation has no usability for multi-objective optimization. As these are then considered basically as one function.

A similar situation as for the offshore wind farm Horn Rev 1 is generated for the investigation. 80 turbines are placed at a fixed distance from each other as shown in Figure 22. The quasi-Monte Carlo method is applied to the given layout and the variance is evaluated. Then the distance is changed and re-evaluated. The distance is first set to 300 meters and then increased by 50 meters after each run up to a maximum distance of 1000 meters. The AEP value increases continuously as the distance increases and the wake effect has less influence on the turbines.

For the evaluation, the AEP power output and the variance were documented. The result can be seen in Figure 22 (right). It can be noted that the variance decreases with increasing AEP power on the x-axis. It can be seen, that the AEP power and the

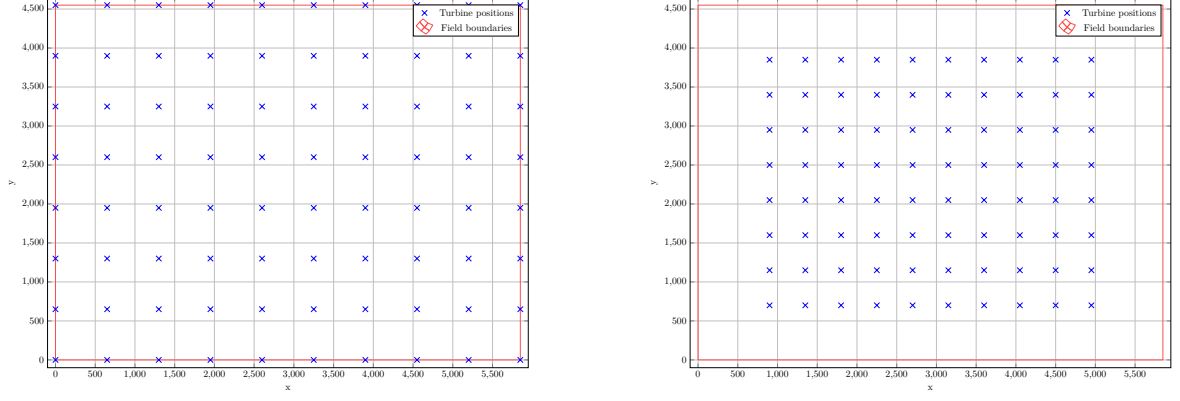


Figure 22: Investigation of variance using different turbine layouts by scaling the distances between the turbines. The left turbine layout was created with a distance of 650 meters between the turbines, while the left layout was created with a distance of only 450 meters. The resulting AEP and variance values can be viewed in Table 3.

Test number	1	2	3	4	5	6
Distance	300	450	600	750	900	1000
AEP value	510653	570361	600885	617033	627224	631927
Variance	1.0468125	1.04144375	1.0320875	1.024825	1.019175	1.01645625

Table 3: AEP and variance results evaluation at different turbine layouts. The distances between the turbines were increased with each test. While the AEP values naturally increase with distance, the variance values continuously decrease. This allows us to conclude that there is a connection between the two values.

variance value do not have a complete linear relationship, but after this test it can be concluded that the general relationship between AEP and variance continues in this manner as visible in Table 3. Consequently, when optimizing for minimum variance as an objective function, the AEP value is increased at the same time. However, this type of optimization is already performed by our first objective function. The result would be the same and thus no multi-objective optimization is possible, because no different optima could be generated.

7.1.3 LCOE with Cabling

This section will provide the details of the LCOE with cable objective function for optimizing and is inspired by the work of Bauer [6] and Cremerius [11]. It is based on the idea of saving costs in the form of cable routing for the transport of electricity between the turbines and integrates these into the LCOE. As explained in Section 3.6.2 the LCOE is the price of electricity per MWh over the lifetime of a wind farm. The initial costs are also integrated, which include, among other things, the costs for



Figure 23: Overview of the different cable distributor stations on- and off-shore. The Offshore Substation is relevant for the optimization of the cable lengths in this thesis, as it connects the cable network to the individual turbines. Source: [1].

the cables.

For cabling of offshore wind farms, it is fundamental to note that the entire system is connected to an onshore substation, which allows electricity to feed into the country's electricity circuit. This is then connected via export cables to an offshore converter, which carries out the high-voltage direct current transmission to the offshore substation. There is not much that can be changed about this previous system, because the electricity has to be transported from the offshore substation to the shore anyway, and the shortest route is simply used for this. Finally, cables are laid from the offshore substation to the individual turbine foundations and at this point the turbine layout has an impact on how much cable needs to be laid. An overview of the different stations can be seen in Figure 23. Thereby not every single turbine foundation has to be connected directly to the substation, instead one cable can connect several turbines to it. This saves installation costs, but the more turbines are connected at the same time, the more power the cable needs to transport. Therefore, in this paper we assume that every cable laid is a comparably strong model.

Clearly, the closer the turbines are placed to the offshore substation, the more the cost of the cable itself and the installation of the cable will decrease. However, it should also be noted that smart positioning of the turbines saves cable length, since, for example, turbine foundations placed in a series require less cable length than turbines positioned in a mixed-up order. And exactly this saving is the focus of this objective function and can be viewed in Figure 24. Since the efficiency of the turbines is in the focus, this optimization function can still save some fundamental costs in the end. In the figure this becomes clear by the left turbine grid in which the turbines are not extended to the entire available area, but are placed closer to the offshore substation. This is also due to the fact that a further distance would only bring about a

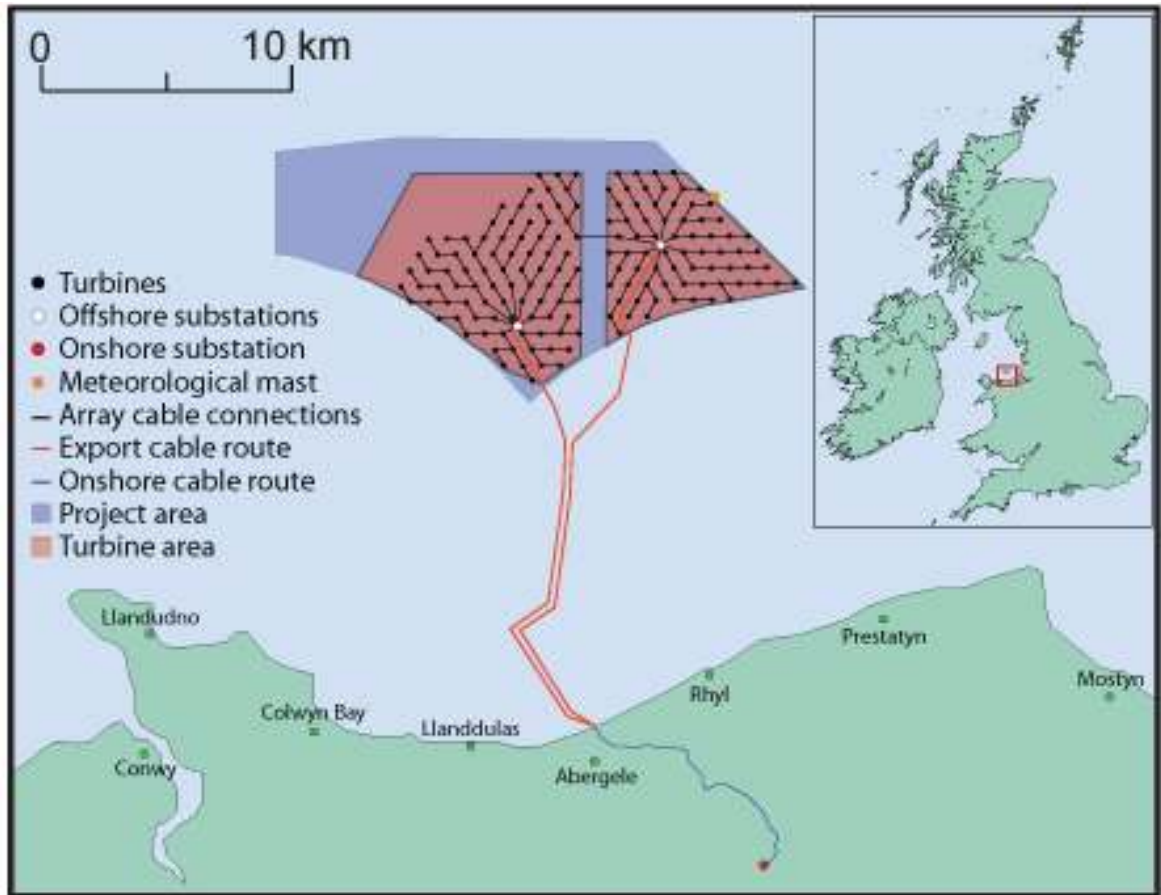


Figure 24: Example of the effect of cable optimization on a real world offshore wind farm. In the left half of the wind farm, not the entire usable area (red) is used to place the turbines (black) as far apart as possible. The turbines are located closer to the offshore substation to save cable material. Source: [35][2].

minimal increase in efficiency while the saving of the cable network has a strong impact.

As you can recognize in the work of Cremerius [11], the topic of cabling and especially the cost-reduced placement of these cables is quite complex. Therefore, with this work we use a simplified strategy to quickly lay a cable network. For this purpose the Minimum Spanning Tree (MST) algorithm connects all positions together, without any cycles and with the minimum possible total length. The root of the MST is the offshore substation from where the MST extends over all turbine foundations. The minimum overall length is now taken as the reference for the cost function. As mentioned before we use a robust cable everywhere which can be priced with about 300000 Euro per kilometre [3]. In addition, there is about 550000 Euro per kilometre for the transport and installation of the cables [11]. That's a total of 850000 euros for every kilometre of cable, which turns out to be a factor not to be underestimated with

Cable cost (€/km)	Installation cost (€/km)	Total (€/km)
300000	550000	850000

Table 4: Breakdown of the various costs of installing cables in an offshore wind farm.
Source: [3] [11]

a larger number of turbines as summarized in Table 4.

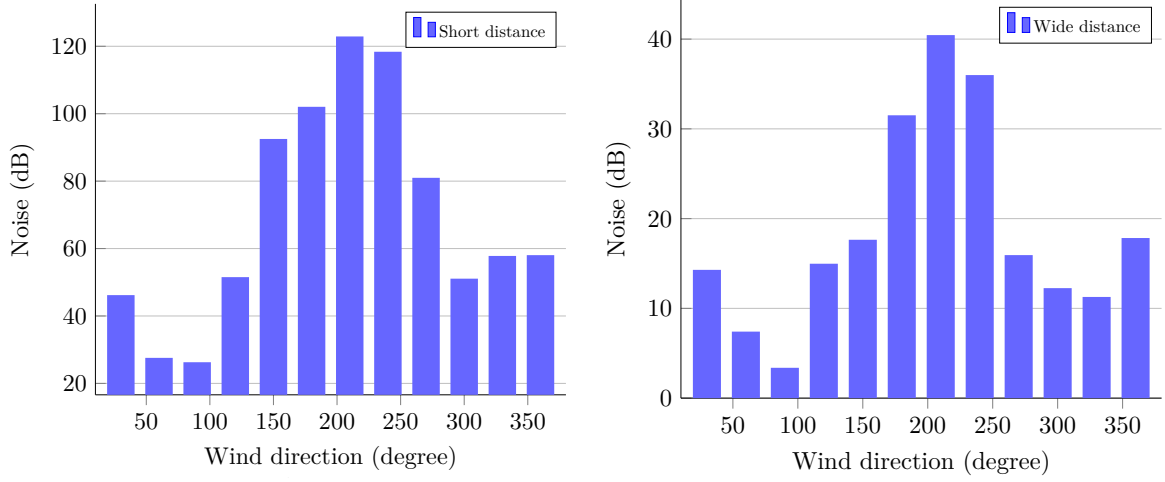
The combined value of total cable costs and the minimum overall length of the MST is now integrated into the LCOE as defined in Section 3.6.2. For this, only the capital costs, which previously included the total construction costs, are being split. Thus, the formula of the LCOE does not need to be further adapted. Finally, the previous LCOE minimization problem is turned into a maximization problem, which can be specified as a percentage. For this purpose, a layout with a minimum distance between the turbines and the substation is selected as the lower bound. The upper barrier, on the other hand, is a very wide-ranging layout, which depends on the rotor diameter. Thus for a new layout always an LCOE value between the two bounds is calculated, which is inverted to maximize the problem during optimization.

7.1.4 Noise Model

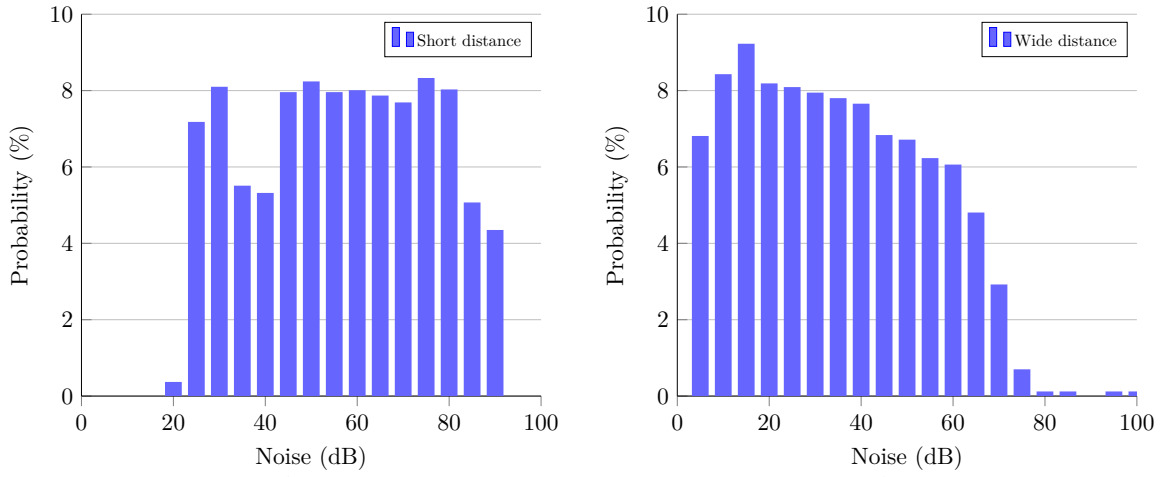
The most common complaint about onshore wind turbines is that they are noisy, which leads to a main focus of public society and a negative view of wind farms. The noises produced are mainly due to modulation associated with the blade passage past the tower and turbulence in the air. The nearest distance that a wind turbine is typically placed to a home is 300 meters or more. At that distance, a turbine will have a sound pressure level of about 43 decibels (dB) [19]. Noise generation is also important for offshore wind farms, as it affects animals and wind farms are also built close to the coast. In addition, that natural ambient noise levels in the ocean are generally much greater than in air. With this background some simple noise calculations have been implemented so that they can be taken into account in multi-objective optimization based on the idea of Kwong [25].

The calculation refers to a specific point and depends on wind speed, observation position, distance and produced sound of the certain turbine type. These parameters are examined in the following. The average noise level over an entire year is of particular interest. The produced noise level of a certain turbine type is fixed throughout the entire calculation and therefore does not need any further investigation. However, the position of the measurement in relation to the turbine is important. Since here, as was made clear in the explanation of the wind model in Section 3.1, the probabilities for the occurrence of a certain direction must be considered. Just like the intensity of the wind speed, as summarized in Figure 25a. It is noticeable that this development is very similar to the wake effect.

The second important parameter is the distance to a wind turbine. However, the noise



(a) Effects of distance on the noise level of the individual wind directions.



(b) Effects of distance on the probabilities of noise level.

Figure 25: Effects of distance on noise level observed over a whole year. The graph on the left shows the noise development at a short distance to the wind farm, while the graph on the right simulates a distant position. As the distance to the wind farm increases, the noise level reduces.

level decreases with further distance as becomes visible for both cases in Figure 25. As well as the probability development for the individual noise intervals in Figure 25b are considered.

7.2 Pareto Frontier

This section defines the Pareto Frontier, also known as Pareto Front or Pareto set. Named after the Italian engineer, sociologist and economist Vilfredo Pareto (1848-1923), this mathematical optimization technique generates a collection of layout samples that provide an optimized result on all given objective functions. A layout sample corresponds to a certain set of turbine positions which are then evaluated with our simulation for the different objective functions. These samples are generated by a local search algorithm, which is described below in Section 7.2.1. So when a new sample is created, it is compared to all other elements from the Pareto Front. The new sample is first added to the set, then all elements are checked for being completely dominated by another sample. In this case, the dominated sample is removed from the Pareto Front. Total dominance is defined such that another sample exceeds the currently evaluated one in all objective functions. Through this filtering process, Pareto Frontier keeps only the best samples of a set, which form the Pareto optimum upon optimization.

To generate such a Pareto optimum there are several optimization algorithms. In this thesis, a property of the neighbourhood optimization of the Local Search is used. Since the layout is fundamentally changed only minimally in each optimization step, it can be assumed that the result of an objective function also changes only minimally compared the previous one.

To achieve this, a tracing approach is applied. The first step is to perform an optimization after each individual objective function. The result of these individual optimizations are the edges of the future Pareto optimum, since it can be supposed that no better individual result can be achieved. Afterwards, an optimization in the direction of every other objective function is carried out with the layout of the edge samples. During these optimizations, the generated sample is checked for total dominance by the Pareto Frontier after each Local Search step. These traces leads gradually to an efficient creation of the Pareto optimum.

In the context of this thesis also a weighted approach was examined. Each objective function is assigned a weight. These weights can change in the course of optimization, but always sum up to one. An iteration step now corresponds to the optimization with the Local Search and all objective functions with a fixed weight which form a connected target function. Now the weights change for the next iteration. Thereby each iteration creates a new element from the Pareto optimum, except if the same weighting is selected twice. This generates a Pareto optimum with strong solutions and has the advantage that it is not necessary to check in every iteration step whether dominated elements exist.

A comparison of the two approaches reveals a fundamental difference in the generation of a Pareto Frontier. With the tracing method, many solutions are generated, some of which are then inserted into the Pareto optimum and others are dominated and discarded. In contrast, the weighted method only generates individual high-quality solutions, which are then all sorted into the Pareto optimum. Thus, the tracing approach generates a dense Pareto optimum in a short time, whereas the weighted approach generates only a small number of results and has a long runtime. In this thesis the tracing approach is further pursued, since a dense Pareto optimum leads to a larger selection of solutions and the running time is a factor not to be underestimated when investigating wind farms with a large number of turbines.

7.2.1 Local Search

At the lowest level of our multi-objective optimization is the Local Search, which generates the different layout samples, that are then examined and compared by the Pareto Frontier explained above. A different type of optimization algorithm could also be used. The Local Search algorithm is a heuristic method for solving computationally hard problems. The algorithm can be applied to any problem that requires a maximum solution as a criterion. Therefore, the declared objective functions have been defined all as maximization problems. Local Search goes step by step through possible solutions and maintains the best one for the next step. A new possible solution is generated by local changes, also known as neighbourhood changes. The algorithm iterates over all turbine positions and moves them minimally around the old position. Then the turbine set is evaluated again and the best solution of both is kept for the next iteration step. The probing of new positions of a certain turbine does not happen randomly, but according to a certain pattern. Circular iteration is performed around the old position in different distances and directions as shown in Figure 26 for 12 wind directions and 5 distances. It becomes clear that the result of an iteration can improve more if a higher number of directions and distances is chosen. However, the complexity of the runtime increases strongly, because a simulation has to be performed for each tested position. The algorithm ends when a certain number of runs has been reached or the result no longer improves significantly.

In this thesis the Local Search variant Simulated Annealing (SA) by Kirkpatrick [24] is used. SA is inspired by the cooling of hot metal. During the annealing the metal changes from liquid to a solid state. The outcome of the annealing process differs with the speed of the cooling. With a slow and controlled cooling a crystalline structure can be achieved. The higher the temperature the faster the atoms move and therefore it is easier to change the structure. The more the temperature decreases the slower the atoms become and it is higher probable that it stays in its current form. Similar to this behaviour in the simulated annealing algorithm it is more likely that a solution will get accepted if the temperature is high. While the temperature decreases the solution space gets more restricted. For our optimization problem it means that solutions can also be accepted which are not significantly better than others, but are

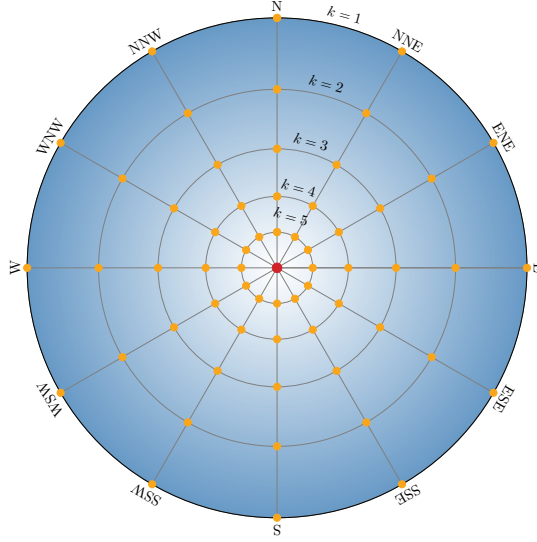


Figure 26: Simulated turbine positions (orange) of the local search for one iteration step and one specific turbine (red). Here with the setting for five different distances and 12 wind directions. At the end, the local search only retains the position with the largest optimum of the entire turbine layout.

still within a certain tolerance range. Especially, for multi-objective optimization this is an important feature, because more solutions are supported where one of the objective functions returns lower scores. As a result, more elements are added to the Pareto Front and the Pareto optimum is given a denser shape [10].

7.3 Results

We run our introduced multi-objective Optimization Algorithm on different test fields and examine them. In our investigation, we proceed in three parts, mainly distinguishing which of the introduced objective functions are included in the multi-objective optimization as target functions. Since the AEP power outcome has a very high priority in the evaluation of every wind farm, this function is always considered. The first two analyses refer to optimizations with two objective functions each, the AEP power and the noise effect or the LCOE with cable. The third analysis will then finally contain all three objective functions at once and demonstrate that the algorithm works with numerous objective functions. The test cases are each executed on a square field with different numbers of turbines. This covers a wide range of different possibilities and it can be assumed that the multi-objective optimization will also be effective in larger fields with a growing number of turbines.

The first test case corresponds to a multi-objective optimization with the AEP power outcome and the noise effect. The field grows proportionally with the number of turbines and the measurement point for the noise effect remains constant at point $(0, 0)$

Test case	1	2	3	4
Turbine number	25	35	45	55
AEP power/Noise test				
Field size ($x = y$)	1400	1800	2200	2600
Noise position	(0, 0)	(0, 0)	(0, 0)	(0, 0)
AEP power/LCOE test				
Field size ($x = y$)	-	2600	3000	3400
Substation position	-	(1100, 1100)	(1300, 1300)	(1500, 1500)

Table 5: Information for the different test cases to evaluate the multi-objective optimizer. Each test case has a certain number of turbines, a field size, a simulated measuring point for the noise effect and a position for the cable substation. Care is taken to ensure that parameters adapt to the number of turbines, so that the results are comparable despite the different number of turbines.

to ensure comparability, as shown in detail in Table 5. The generated Pareto optima for the different number of turbines can be seen in Figure 27. First of all, it is clear that all four test cases have a similar course. This is also intended and verified that the optimization can also handle other inputs such as turbines, number and size of the field and will still have a comparable curve. The AEP power fluctuates in a strong range in contrast to the noise effect, which is due simply to the fact that the AEP value depends significantly on the number of turbines and also the maximum achievable AEP differs in the various test cases. If the graph were not displayed with the final power values but with the percentage values, as in Figure 29 for example, the four curves would lie slightly above each other.

In contrast to the AEP, the noise value for all test cases is in a similar range. This is because we have chosen the measuring point constant and this provides the same values when the turbines are positioned nearby. However, it is also noticeable that the 45 turbines with the largest field can achieve the lowest noise value, which is due to the fact that the turbines can be positioned further away from the measuring point on a larger field. On the other hand, it can be observed that the highest noise value fluctuates strongly and only increases with larger gaps as the AEP power grows. This occurs to varying intensities in the test cases, since the abort criterion of local search declares the algorithm complete if the efficiency growth is too low.

In summary, the resulting Pareto optima are all in a rather strong curved form, which suggests that the two objective functions do not work completely against each other, but that good coexistent solutions exist. Which ensures a good AEP efficiency of the turbines, but can still keep the noise factor low.

The second test case corresponds to a multi-objective optimization with AEP power efficiency and the lowest possible LCOE. The field again grows proportionally to the number of turbines. However, the position of the offshore substation changes, so that in relation to the field size it is approximately at the same position in the lower left

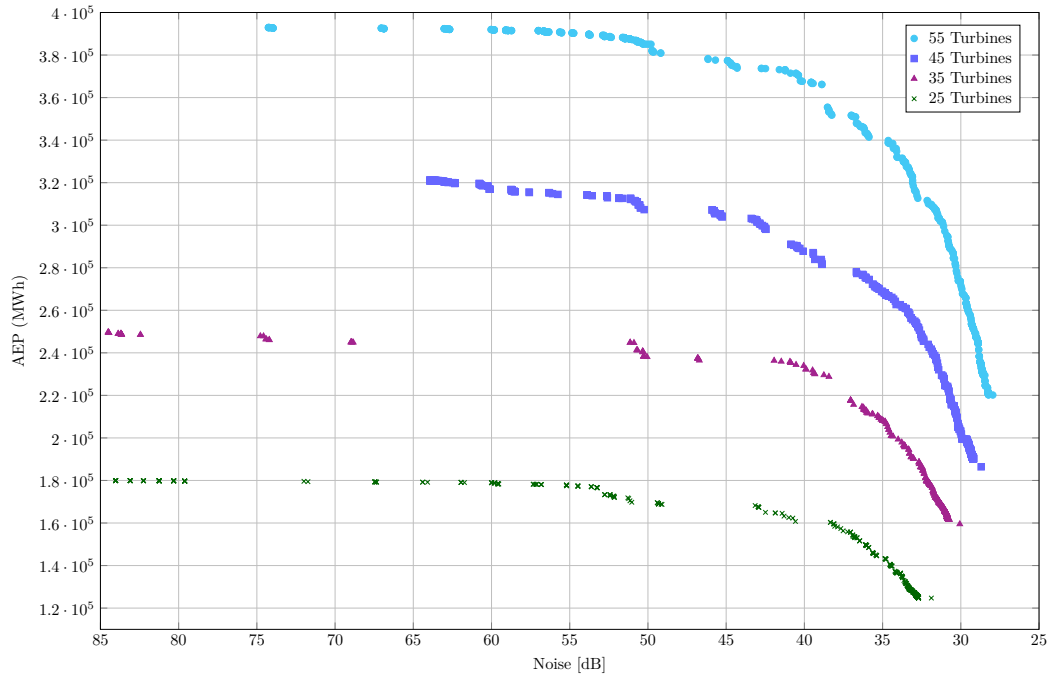


Figure 27: Evaluation of Pareto optima with AEP value and noise effect for different numbers of turbines. The result is curve-like for all evaluations, which indicates a relatively good interaction between the two objective functions

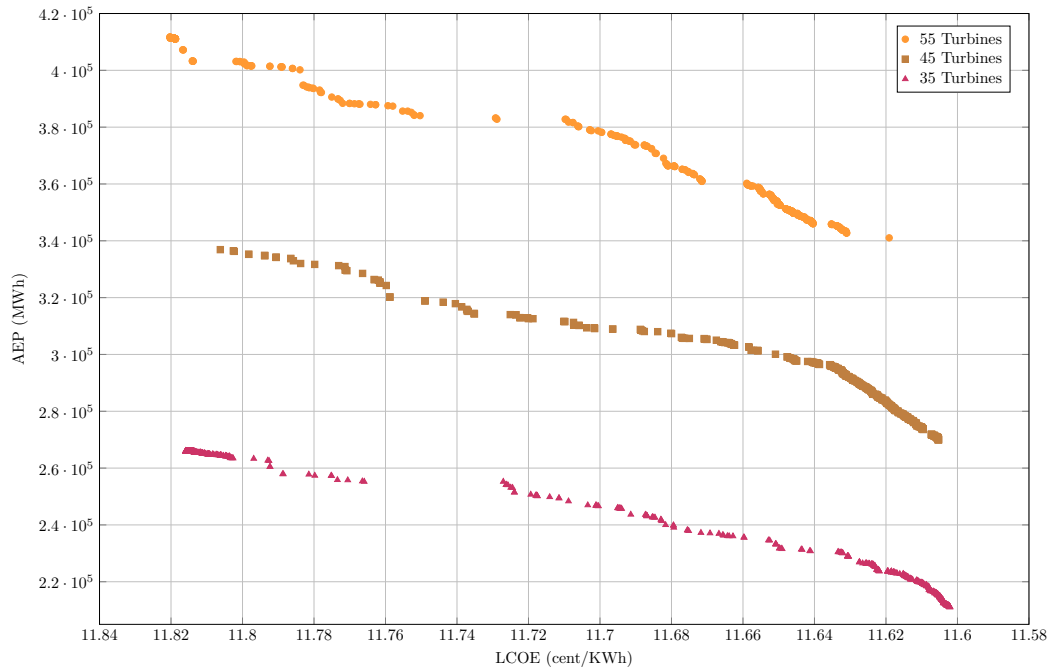


Figure 28: Evaluation of Pareto optima with AEP value and LCOE for different numbers of turbines. The result has a relatively linear form in all evaluations, which indicates that the two objective functions do not interact so well.

AEP power/Noise/LCOE test			
Turbine number	Field size ($x = y$)	Noise position	Cable Substation
50	2000	(1200, 0)	(400, 400)

Table 6: Settings for the investigation of the multi-objective optimizer with three target functions. The number of turbines and the field size were selected for the general settings. For the LCOE a specific position of the substation was chosen and for the Noise Effect a measuring point.

quarter. The exact data can be found in Table 5. Since economic values of a wind farm are required for the calculation of the LCOE, the data of the offshore wind farm Horns Rev is used and scaled to the number of turbines. As a result, the calculated LCOE is in the same range for all test cases. The resulting Pareto optima can be seen in Figure 28. During the evaluation, similar characteristics as in the first test case can be observed. The AEP power value differs significantly due to the different number of turbines.

For the LCOE it can be observed that the value itself only changes in a minor range. This is because the cable costs are only considered as part of the initial construction costs of a wind farm in the LCOE. As a consequence, the results due to changes in cable costs are minimal. Nevertheless, these small fluctuations should not be underestimated in the extrapolation. In addition, it is noticeable that the improvement of the LCOE is consistent, which is due to the fact that the given field is quadratic and therefore the cable network is not faced with any exceptional cases.

Overall, it is remarkable that in contrast to the first test case, the Pareto optima is not curved rather linear. This suggests that the two objective functions act more strongly against each other to achieve good results. On closer inspection, it is due to the characteristic that a good LCOE is largely based on the fact that the turbines are close to each other, thereby reducing the overall cable length. In contrast, the AEP power outcome is dependent on the turbines being further apart, thus weakening the wake effect. Therefore, when selecting an element from the Pareto optimum, it should be noted that it comes from the upper part of the AEP efficiency, since there the desired effect of a high AEP occurs with a slightly cable network oriented layout, as explained in Section 7.1.3.

The third test case now contains all three introduced objective functions at once. This time a specific number of turbines and a field size will be investigated. The exact information can be found in Table 6. The resulting Pareto optimum can be seen in Figure 29. In the graph, the first two objective functions are plotted as usual on the x and y axis, while the third function is represented as a color with the corresponding colorbar on the right side. In addition, this graph does not convert the percentage value of the target functions to the real values. Which does not change the shape of the Pareto front and gives an idea of the percentage scaling of the objective functions. In contrast to the other two test cases, this Pareto optimum has no uniform shape,

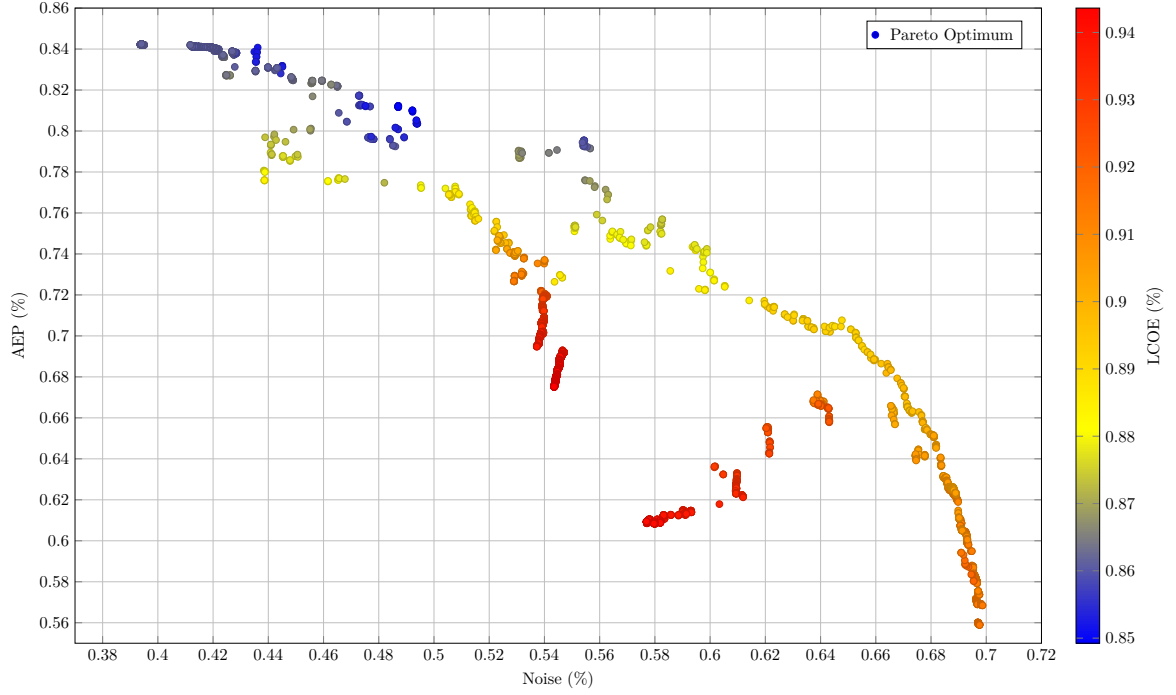


Figure 29: Examination of the Pareto optimum with three objective functions at once plotted in a 2D graph. The evaluation of the target functions is given in percent as for the multi-objective optimizer for a 50 turbines layout. The colors represent the LCOE value of the respective turbine layout according to the right color scheme.

neither curved nor linear. Since the three objective functions expand in a certain direction, it becomes clear how the AEP expands to the top left and the noise effect to the bottom right. However, the LCOE expands downwards in the middle of the graph by two ropes, which are illustrated by the red dots. This is due to the fact that both the AEP and the noise effect decrease as the LCOE improves. The two ropes clearly show how each was optimized from one direction.

On closer inspection, the previously made findings will be confirmed once again. The AEP value and the noise effect form a curved line in the Pareto optimum and a good AEP value in the upper left corner gets bad LCOE results. However, the noise effect and the LCOE with cable can coexist well, as shown by the orange dots in the lower right corner. In addition, some peaks can be detected compared to the multi-objective optimization with two functions.

7.4 Performance on Real World Wind Farms

In the last part of this section the multi-objective Optimizer is applied to the real wind farm scenarios of Horns Rev 1, Sandbank and DanTysk. This means that the same field boundaries, turbine types, economic values and basic settings are used. Each wind farm once with AEP and noise effect as object functions as well as AEP and LCOE.

Wind farm	AEP power (MWh)	Efficiency (%)	LCOE (cent/kWh)	NPV
Horns Rev 1	578362	88.5119	12.1475	−100.749
Sandbank	1290810	92.6519	8.06855	948.31
DanTysk	1251560	94.2726	9.20149	521.498

Table 7: Simulation results of different cost models with original turbine layouts for the three real-world wind farms.

Graphically the dots of the Pareto optimum are colored and the dominated elements are shown in grey. To compare the results, the simulated values of the original turbine positions can be found in Table 7.

7.4.1 Horns Rev 1

The offshore wind farm Horns Rev is placed in the North Sea and was build in three phases. Here we look at the first built part, the Horns Rev 1. This was the first large scale offshore wind farm of the world, build in 2002. The wind farm has a total of 80 Vestas V80-2.0 MW turbine units installed. Originally the turbines are laid out as an oblique rectangle of $5\text{km} \times 3.8\text{km}$ and the distance between the turbines is constant 560 m in both directions.

In the first multi-objective optimization the objective functions AEP efficiency and noise were used, the resulting Pareto optimum can be examined in Figure 30 (left). The measurement position for the noise level was set to (6000, 0), which is the lowest right corner of the field. At closer inspection a well consistent Pareto optimum (blue dots) curve can be seen. Thereby the edges of the front range from a noise minimum of 25 dB to an AEP maximum of just over 600 MWh. The dominated elements (gray) are most near the Pareto optima, which suggests that most of the steps in the optimization were sensible and in the right direction. Only a few elements are offside and correspond to redundant iteration steps.

The optimization of AEP efficiency and LCOE, on the other hand, forms a wider spectrum of dominated elements as visible in Figure 30 (right). This indicates that in this case it was much more difficult for the algorithm to find a solution that matches both objective functions. The similar nature of the Pareto optimum to the previously generated test cases also indicates this. Here a quite linear Pareto optimum with a very slight curvature is recognizable. However, the jump in the upper left corner, which increases the AEP again by 10000, and the large number of dominated elements in this area is conspicuous.

In summary, the optimizer delivers a strong Pareto optimum in both cases, which are characterized by a dense behavior. Consequently, from a large number of new layout solutions for Horns Rev 1 can be chosen, which consider two objective functions.

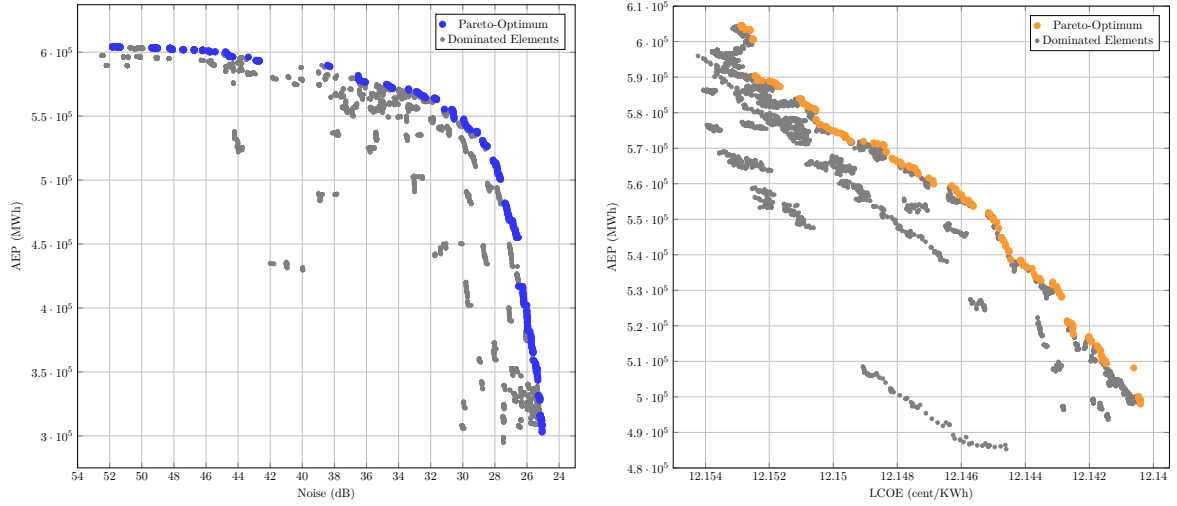


Figure 30: Evaluation of the multi-objective optimization for Horns Rev 1. On the left side for AEP and noise and on the right side for AEP and LCOE as objective functions. The colored elements correspond to the Pareto optimum and the grey points to the dominated turbine layouts, whose simulated values were superior during the optimization.

7.4.2 Sandbank

Sandbank is an offshore wind farm which is located about 90 kilometres west of the island of Sylt and covers an area of 59km². In this thesis we consider the first development stage with 72 wind turbines of the type Siemens SWT-4.0-130. The field corresponds to an elongated parallelogram with a width of about 3.5km and a length of 19km. The noise measuring point was set to (6500,0) at the lowest point of the usable area and the offshore substation was set to (3500,9500) by estimation of the original Sandbank turbine map.

The results of the multi-objective optimization are visible in Figure 31 (left). In the first optimization case it can be observed that the Pareto optimum has a gap at the top where a strong loss of the noise effect results from the slightly increasing AEP. On its other side it also becomes visible that only by strong restrictions of the AEP value small improvements of the noise are achieved. Consequently, there can be spoken of a hard curve of the Pareto optimum, where the sides run straight and the actual curve takes place in a small area. Also noticeable is a small jump in the middle of the Pareto optimum, in which the dominated elements show how the iterations have proceeded in the optimization. Overall, the dominated elements are all very close to the optima, which speaks for an effective optimization process.

The second optimization with LCOE in Figure 31 (right) has a similarly good convergence of the dominated elements to the Pareto optimum with the exception of a series in the lower field area. Overall, the Pareto optimum is very densely distributed and has no gaps.

In summary, the optimizer worked very efficiently in both cases with barely any un-

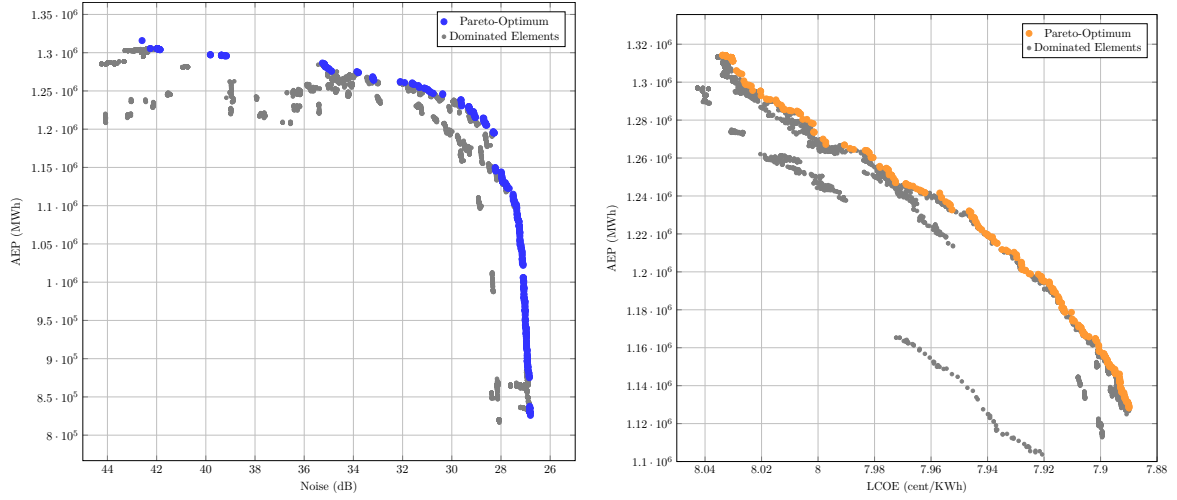


Figure 31: Evaluation of the multi-objective optimization for Sandbank. On the left side for AEP and noise and on the right side for AEP and LCOE as objective functions. The colored elements correspond to the Pareto optimum and the grey points to the dominated turbine layouts, whose simulated values were superior during the optimization.

necessary samples.

7.4.3 DanTysk

The offshore wind farm DanTysk, which is located about 70 km west of the island of Sylt and covers an area of 71 km², has been producing electricity for the German power network since 2014. 80 Siemens SWT-3.6-120 turbines are installed on a long triangular shaped field with a width of 5 km and a length of 19 km. The field is more challenging than the previous two, as there is still a restricted area in the upper part of the area. The noise measuring point was set to (5000, 0) into the lower right corner of the field and the offshore substation was set to (4000, 7000) by estimation of the original DanTysk turbine layout.

During the evaluation of the first multi-objective optimization in Figure 32(left) it is noticeable that there are many dominated elements in the upper half of the AEP peak. Also a gap is to be discovered in the Pareto optimum in the upper part. This indicates that many samples were created to achieve a high AEP power value. In contrast, on the noise side a very linear sequence of optima can be seen, similar to the optimization of the sandbank. This makes the fluctuation of the AEP value, seen in the overall evaluation, very strong. For this reason a solution from the upper quarter should be chosen for a final selection from the Pareto optimum.

In the second optimization, as shown in Figure 32(right), the distribution of the dominated elements is stronger than in the sandbank analysis, but still in a good range, as only one row in the lower part is noticeable again. The Pareto optimum is densely

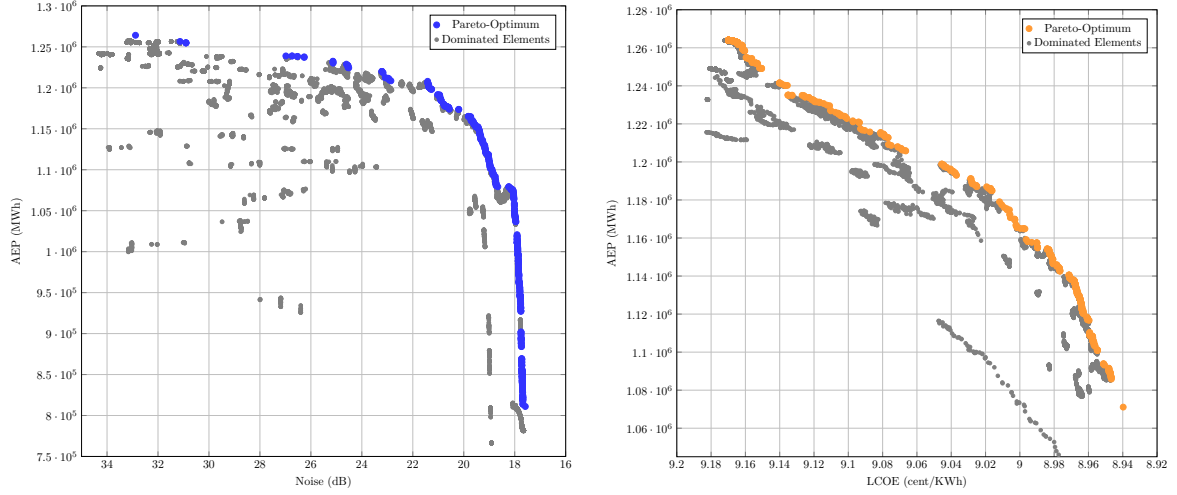


Figure 32: Evaluation of the multi-objective optimization for DanTysk. On the left side for AEP and noise and on the right side for AEP and LCOE as objective functions. The colored elements correspond to the Pareto optimum and the grey points to the dominated turbine layouts, whose simulated values were superior during the optimization.

distributed without large gaps.

A general comparison of all three wind farms shows that the AEP value for optimization with noise effect always fluctuates much more strongly than for LCOE optimization. Thus, the final selection should always be made from the solutions of the upper quarter. Furthermore, the LCOE Pareto optima is denser and without jumps at the Sandbank and DanTysk wind farms, where the offshore substation position is close to the real position. In contrast to Horns Rev 1, where the substation position was chosen more randomly. In summary, the multi-objective Optimizer provides a set of good solutions for the real-world wind farms, with even better results than for the original layouts by the combination of two objective functions.

8 Conclusion and Future Works

In this thesis both the model side and the optimizer side of offshore and onshore wind farms are covered. First the simulation is considered and a time-dependent power production is introduced to consider the effects of different energy prices. The investigation has shown that optimization with time-dependent prices has an influence on the layout of the turbines. In order to distinguish the individual time intervals, the raw data were examined more closely and used more accurately. A future expansion would be the additional differentiation into months or seasons, since the influence of Solar Energy on the energy price in winter is smaller.

These more accurate raw data measurements are also used for the new method of AEP calculation. It was analysed how exactly the FINO3 measurement data are structured and from which wind directions and wind speeds most energy follows. For the implemented calculations, it is possible to choose between Nearest Neighbour and Bilinear Interpolation. The comparison with the standard method has shown that the new calculation comes much closer to the exact result. In addition, the investigation turned out that a more exact resolution of the simulated wind speeds has hardly any effect. However, the resolution of the wind directions has a very large effect on the result.

As next topic uncertainties were discovered and the multi-level Monte Carlo as well as the quasi-MLMC method were introduced for a more accurate evaluation of perturbed input variables. Compared to the classic Monte Carlo methods, the two new algorithms have the advantage that no exact input parameters, such as the sample size, are required and a satisfactorily accurate result is always achieved. In the future, an investigation of the influence of each individual input parameter on the final result can be performed with the MLMC methods.

Last but not least, a multi-objective optimizer is introduced which generates a set of optimal solutions with several target functions and is applied to the real-world wind farms Horns Rev 1, Sandbank and DanTysk. The target functions used in this thesis are power generation, LCOE costs and noise generation. The result of our multi-objective optimizer is a continuous Pareto front with only few gaps, regardless of the selected target functions. This allows an exact result to be chosen according to one's own wishes.

Further work in this topic area would be the inclusion of new objective functions, such as CO2 emission [7][15] or the consideration of the cable power loss [16], as well as an extension of the single optimizer used. An evolutionary approach, such as the NSGA-II algorithm, would be suitable for this, since it already achieves verifiably good results by an efficient simultaneous calculation of several Pareto optima at once [12]. Especially since this topic has recently been properly explored, there are still some extensions and investigations that can be done.

References

- [1] Grid connection. <https://www.nordseeone.com/wind-farm/power-connection.html>. Accessed: 2019-01-23.
- [2] Emperor cable cleats chosen for gwynt y môr offshore wind farm. <https://www.etscablecomponents.com/2013/07/emperor-cable-cleats-chosen-gwynt-y-mor-offshore-wind-farm/>. Accessed: 2019-01-23.
- [3] Submarine power cables. <http://www.nexans.no/Germany/2013/SubmPowCablesFINAL10jun13engl.pdf>. Accessed: 2019-01-26.
- [4] M. Abramowitz and I. Stegun. *Handbook of mathematical functions: with formulas, graphs, and mathematical tables*, volume 55. Courier Corporation, 1965.
- [5] R. J. Barthelmie, G. C. Larsen, S. T. Frandsen, L. Folkerts, K. Rados, S. C. Pryor, B. Lange, and G. Schepers. Comparison of wake model simulations with offshore wind turbine wake profiles measured by sodar. *Journal of Atmospheric and Oceanic Technology*, 23(7):888–901, 2006. doi: 10.1175/JTECH1886.1.
- [6] J. Bauer and J. Lysgaard. The offshore wind farm array cable layout problem: a planar open vehicle routing problem. *Journal of the Operational Research Society*, 66(3):360–368, 2015.
- [7] B Ould Bilal, V Sambou, CMF Kébé, PA Ndiaye, and M Ndongo. Methodology to size an optimal stand-alone pv/wind/diesel/battery system minimizing the levelized cost of energy and the co2 emissions. *Energy Procedia*, 14:1636–1647, 2012.
- [8] R. Cakar. Uncertainty quantification of wind farm models. Bachelor thesis, RWTH Aachen University, 2017.
- [9] J. Choi and M. Shan. Advancement of jensen (park) wake model. In *Proceedings of the European Wind Energy Conference and Exhibition*, pages 1–8, 2013.
- [10] Y. Collette and P. Siarry. *Multiobjective optimization: principles and case studies*. Springer Science & Business Media, 2013.
- [11] P. Cremerius. Optimal cable layout for offshore wind farms by integer linear optimization. page 71, 2016.
- [12] K. Deb, S. Agrawal, A. Pratap, and T. Meyarivan. A fast elitist non-dominated sorting genetic algorithm for multi-objective optimization: Nsga-ii. In *International Conference on Parallel Problem Solving From Nature*, pages 849–858. Springer, 2000.

- [13] Kalyanmoy Deb. Multi-objective optimization. In *Search methodologies*, pages 403–449. Springer, 2014.
- [14] DNV. Framework for the categorisation of losses and uncertainty for wind energy assessments. Technical report, KEMA, 2013.
- [15] R. Dufo-López and J. L. Bernal-Agustín. Multi-objective design of pv–wind–diesel–hydrogen–battery systems. *Renewable energy*, 33(12):2559–2572, 2008.
- [16] M. Fischetti and D. Pisinger. Optimizing wind farm cable routing considering power losses. *European Journal of Operational Research*, 08 2017. doi: 10.1016/j.ejor.2017.07.061.
- [17] M. B. Giles. Multilevel monte carlo methods. In *Monte Carlo and Quasi-Monte Carlo Methods 2012*, pages 83–103. Springer, 2013.
- [18] D. Guirguis, D. A. Romero, and C. H. Amon. Toward efficient optimization of wind farm layouts: Utilizing exact gradient information. *Applied Energy*, 179:110 – 123, 2016. ISSN 0306-2619.
- [19] J. P. Harrison. Wind turbine noise. *Bulletin of Science, Technology & Society*, 31 (4):256–261, 2011.
- [20] G. Heiming. Modeling and simulation of offshore wind farms. Bachelor thesis, RWTH Aachen University, 2015.
- [21] T. J. Sullivan. *Introduction to Uncertainty Quantification*. Springer, Heidelberg, New York, Dordrecht, 2015.
- [22] N. O. Jensen. *A Note on Wind Generator Interaction*. Number 2411 in Risø-M. Risø National Laboratory, Roskilde, 1983.
- [23] I. Katic, J. Højstrup, and N. O. Jensen. A simple model for cluster efficiency. In *European wind energy association conference and exhibition*, pages 407–410, 1986.
- [24] S. Kirkpatrick, C. D. Gelatt, and M. P. Vecchi. Optimization by simulated annealing. *science*, 220(4598):671–680, 1983.
- [25] W. Y. Kwong, P. Y. Zhang, D. Romero, J. Moran, M. Morgenroth, and C. Amon. Wind farm layout optimization considering energy generation and noise propagation. In *ASME 2012 International Design Engineering Technical Conferences and Computers and Information in Engineering Conference*, pages 323–332. American Society of Mechanical Engineers, 2012.
- [26] M. A. Lackner and C. N. Elkinton. An analytical framework for offshore wind farm layout optimization. *Wind Engineering*, 31(1):17–31, 2007. doi: 10.1260/030952407780811401. URL <https://doi.org/10.1260/030952407780811401>. Accessed: 02.05.2018.

- [27] B. Lange, H.-P. Waldl, A. G. Guerrero, D. Heinemann, and E. J. Barthelmie. Modelling of offshore wind turbine wakes with the wind farm program flap. *Wind Energy: An International Journal for Progress and Applications in Wind Power Conversion Technology*, 6(1):87–104, 2003.
- [28] W. J. Morokoff and R. E. Caflisch. Quasi-monte carlo integration. *Journal of Computational Physics*, 122(2):218 – 230, 1995.
- [29] N. G. Mortensen, D.N. Heathfield, O. Rathmann, and M. Nielsen. Wind atlas analysis and application program: Wasp 11 help facility, 2014.
- [30] G. Mosetti, C. Poloni, and B. Diviacco. Optimization of wind turbine positioning in large windfarms by means of a genetic algorithm. *Journal of Wind Engineering and Industrial Aerodynamics*, 51(1):105–116, 1994.
- [31] p. Bratley and B. L. Fox. Algorithm 659: Implementing sobol’s quasirandom sequence generator. *ACM Trans. Math. Softw.*, 14(1):88–100, March 1988.
- [32] M. Pisaroni, S. Krumscheid, and F. Nobile. Quantifying uncertain system outputs via the multilevel monte carlo method–part i: Central moment estimation. Technical report, 2017.
- [33] S. Raychaudhuri. Introduction to monte carlo simulation. In *Proceedings of the 40th Conference on Winter Simulation*, WSC ’08, pages 91–100. Winter Simulation Conference, 2008.
- [34] P. Richter, J. Wolters, R. Cakar, A. Verhoeven-Mrosek, and M. Frank. Uncertainty quantification of offshore wind farms. John Wiley & Sons, 2017.
- [35] S. Rodrigues, C. Restrepo, E. Kontos, R. Teixeira Pinto, and P. Bauer. Trends of offshore wind projects. *Renewable and Sustainable Energy Reviews*, 49: 1114 – 1135, 2015. ISSN 1364-0321. doi: <https://doi.org/10.1016/j.rser.2015.04.092>. URL <http://www.sciencedirect.com/science/article/pii/S1364032115003627>.
- [36] S. Rodrigues, P. Bauer, and P. A. Bosman. Multi-objective optimization of wind farm layouts–complexity, constraint handling and scalability. *Renewable and Sustainable Energy Reviews*, 65:587–609, 2016.
- [37] B. Roscher, F. Harzendorf, R. Schelenz, and G. Jacobs. Reduced levelized cost of energy through optimization of tower height, rotor diameter and wind farm layout. *American Journal of Engineering Research (AJER)*, 7(4):130–138, 2018. ISSN 2320-0847.
- [38] M. Samorani. The wind farm layout optimization problem. In *Handbook of Wind Power Systems*, pages 21–38. Springer, 2013.

- [39] R. C. Smith. *Uncertainty Quantification: Theory, Implementation, and Applications*. Society for Industrial and Applied Mathematics, Philadelphia, PA, USA, 2013.
- [40] A. Tesauro, P.-E. Réthoré, and G. C. Larsen. *State of the art of wind farm optimization*, chapter 0, page 11. European Wind Energy Association (EWEA), 2012.
- [41] A. Tuzuner and Z. Yu. A theoretical analysis on parameter estimation for the weibull wind speed distribution. In *Power and Energy Society General Meeting- Conversion and Delivery of Electrical Energy in the 21st Century, 2008 IEEE*, pages 1–6. IEEE, 2008.
- [42] J. Wiernga. Representative roughness parameters for homogeneous terrain. *Boundary-Layer Meteorology*, 63(4):323–363, 1993.